ChemPubSoc Europe

DOI: 10.1002/chem.201605070

CHEMISTRY A European Journal Full Paper

Polyoxometalates

Structural Transformation from Dimerization to Tetramerization of Serine-Decorated Rare-Earth-Incorporated Arsenotungstates Induced by the Usage of Rare-Earth Salts

Hai-Lou Li,[a, b] Ya-Jie Liu,[a] Jing-Lin Liu,[a] Li-Juan Chen,[a] Jun-Wei Zhao,*[a] and Guo-Yu Yang*[b]

Abstract: Three types of serine-decorated rare-earth-containing arsenotungstate $[H_2N(CH_3)_2]_6NaH[RE_2W_4O_{10}(H_2O)_8(Ser)_2(B\text{-}\alpha\text{-}AsW_9O_{33})_2]\cdot 30H_2O$ ($RE^{3+}=Eu^{3+}$, Gd^{3+}, Tb^{3+}, Dy^{3+}, Ho^{3+}, Er^{3+}, Tm^{3+}, Yb^{3+}, and Y^{3+}; **1**), $[H_2N(CH_3)_2]_6Na_{6-x}RE_xH_{4-2x}[RE_4W_8O_{19}(H_2O)_{10+y}(OH)_2(Ser)_2(B\text{-}\alpha\text{-}AsW_9O_{33})_4]\cdot nH_2O$ ($RE^{3+}=Tb^{3+}$, $x=1$, $y=2$, $n=36$; $RE^{3+}=Dy^{3+}$, Ho^{3+}, Er^{3+}, Yb^{3+}, Y^{3+}, $x=0$, $y=0$, $n=38$; $RE^{3+}=Tm^{3+}$, $x=1$, $y=0$, $n=38$; Ser = serine; **2**), and $[H_2N(CH_3)_2]_{6-2x}Na_{2+3x}RE_xH_{10-6x+y}[RE_4W_8O_{19}(H_2O)_8(OH)_2(Ser)_4(B\text{-}\alpha\text{-}AsW_9O_{33})_4]\cdot Cl_y\cdot nH_2O$ ($RE^{3+}=Ce^{3+}$, Pr^{3+}, $x=1$, $y=0$, $n=65$; $RE^{3+}=Nd^{3+}$, Sm^{3+}, $x=0$, $y=0$, $n=65$; $RE^{3+}=Eu^{3+}$, Gd^{3+}, $x=1$, $y=2$, $n=45$; **3**) were synthesized with the participation of the organic solubilizers dimethylamine hydrochloride and L-serine and were structurally characterized. The use of different amounts of rare-earth salts results in the structural transformation from dimerization to tetramerization of types **1**–**3**. Type **1** is a dimeric sandwich-type assembly of a dual-Ser-participating $[RE_2W_4O_{10}(H_2O)_8(Ser)_2]^{10+}$ entity sandwiched by two $[B\text{-}\alpha\text{-}AsW_9O_{33}]^{9-}$ moieties, whereas types **2** and **3** have a tetrameric square structure formed by four $[B\text{-}\alpha\text{-}AsW_9O_{33}]^{9-}$ moieties that anchor a dual/tetra-Ser-participating $[RE_4W_8O_{19}(H_2O)_{10+y}(OH)_2(Ser)_2]^{20+}$ or $[RE_4W_8O_{19}(H_2O)_8(OH)_2(Ser)_4]^{20+}$ core. The solid-state luminescence properties and lifetime–decay behaviors of these compounds were investigated. The chromaticity coordinates, dominant wavelengths, color purities, and correlated color temperatures were also calculated.

Introduction

Polyoxometalate (POM)-based materials have displayed multiple potential applications in catalysis, medicine, magnetism, gas sorption, molecular recognition, electronics, and nonlinear optics.[1] These materials are closely related to their anionic cluster frameworks that show several noticeable features: 1) the ability to maintain a high integrity in the solid state and aqueous solution; 2) the ability to display various species with a wide range of sizes, shapes, and even highly symmetric topologies; 3) the possession of interesting electronic properties (e.g., the storage of various numbers of electrons without fundamental structure changes, thus leading to the mixed-valence system in which the extra electrons are extensively delocalized over the whole POM skeleton); 4) the ability to act as multidentate inorganic ligands to incorporate either functional organic moieties or second metal centers from the d and f blocks.[2]

Among these compounds, arsenotungstates (ATs) are an important subfamily with a wide range of diverse structures and properties and that have attracted increasing interest over several decades (Table S1 in the Supporting Information). Between 2009–2014, Boskovic and co-workers reported some great achievements in the field of organic-ligand-functionalized rare-earth (RE)-containing ATs (RECATs), which were obtained from the conventionally used acidic aqueous solution by employing the versatile precursors $[As_2W_{19}O_{67}(H_2O)]^{14-}$ and $[B\text{-}\alpha\text{-}AsW_9O_{33}]^{9-}$.[3–9] Some typical examples include acetate-containing $[Yb_{10}As_{10}W_{88}O_{308}(OH)_8(H_2O)_{28}(OAc)_4]^{40-}$,[3] 1D chainlike $[Dy_4As_2W_{22}O_{76}(H_2O)_{19}(C_2H_5NO_2)_2]^{2-}$,[4] the organically sensitizing luminescent $[Tb_8(pic)_6(H_2O)_{22}(B\text{-}\beta\text{-}AsW_8O_{30})_4(WO_2(pic)_6]^{12-}$ (pic = 2-picolinate),[5] glycine (Gly)-encapsulating $[Dy_4As_5W_{40}O_{144}(H_2O)_{10}(Gly)_2]^{21-}$ with single-molecule magnet (SMM) characteristics,[6] and the 3D framework $[K_2\{Dy(H_2O)_3\}_2As_2W_{19}O_{68}][WO_2(pic)]_2]^{6-}$.[7] Recently, Niu and co-workers have been very active in the research of ATs[10–18] and have addressed several classes of RECAT–carboxylate hybrid, such as pydc-containing $[As_6W_{58}O_{206}Ce_4(pydc)(H_2O)_6]^{38-}$ (H_2pydc = pyridine-2,3-dicarboxylic acid),[12] tartrate-bridging $[RE_2(C_4H_4O_6)(C_4H_2O_6)(AsW_9O_{33})]_2^{18-}$ ($RE^{3+}=Ho^{3+}$, Er^{3+}, Tm^{3+}, Yb^{3+}, Lu^{3+}, and Y^{3+}),[14] citrate-functionalized

[a] H.-L. Li, Y.-J. Liu, J.-L. Liu, Dr. L.-J. Chen, Prof. Dr. J.-W. Zhao
Henan Key Laboratory of Polyoxometalate Chemistry
Institute of Molecular and Crystal Engineering
College of Chemistry and Chemical Engineering
Henan University, Kaifeng, Henan 475004 (P.R. China)
E-mail: zhaojunwei@henu.edu.cn

[b] H.-L. Li, Prof. Dr. G.-Y. Yang
MOE Key Laboratory of Cluster Science, School of Chemistry
Beijing Institute of Technology, Beijing 100081 (P.R. China)
E-mail: ygy@bit.edu.cn

Supporting information for this article can be found under http://dx.doi.org/10.1002/chem.201605070.

$[RE_3(H_2O)_7\{RE_2(H_2O)_4As_2W_{19}O_{68}(WO_2)_2(C_6O_7H_4)_2\}_3]^{33-}$ (RE^{3+} = Y^{3+}, Tb^{3+}, Dy^{3+}, Ho^{3+}, Er^{3+}, Tm^{3+}, Yb^{3}, and Lu^{3+}),[15] and the double-malate-connective $[(RE_3(\mu_3\text{-}OH)(H_2O)_8(AsW_9O_{33})\{AsW_{10}O_{35}(mal)\}_2]^{22-}$ (RE^{3+} = Dy^{3+}, Tb^{3+}, Gd^{3+}, Eu^{3+}, and Sm^{3+}).[16] Kortz et al. reported several AT-based organo-tin derivatives, such as bis-phenyltin- or dimethyltin-containing $[(C_6H_5Sn)_2As_2W_{19}O_{67}(H_2O)]^{8-}$[19] and $[\{Sn(CH_3)_2(H_2O)\}_2\{Sn(CH_3)_2\}As_3(\alpha\text{-}AsW_9O_{33})_4]^{21-}$,[20] and a Ti_7-incorporating $[Ti_6(TiO_6)(AsW_9O_{33})_4]^{20-}$.[21] Over 2009–2011, Patzke and co-workers reported an unusual Gd^{3+}-bridging AT nanocluster $[Gd_8As_{12}W_{124}O_{432}(H_2O)_{22}]^{60-}$,[22] a family of Cs^+-templated RECATs $[Cs\subset RE_6As_6W_{63}O_{218}(H_2O)_{14}(OH)_4]^{25-}$ (RE^{3+} = Eu^{3+}, Gd^{3+}, Tb^{3+}, Dy^{3+}, Ho^{3+}, and Er^{3+}),[23] and a class of nanocluster $[RE_{16}As_{16}W_{164}O_{576}(OH)_8(H_2O)_{42}]^{80-}$ (RE^{3+} = Eu^{3+}, Gd^{3+}, Tb^{3+}, Dy^{3+}, and Ho^{3+}) with an investigation into the magnetic properties of the Gd^{3+}-containing member.[24] Wang and co-workers discovered an alanine-decorated cryptand AT $[Ce_4As_4W_{44}O_{151}(ala)_4(OH)_2(H_2O)_{10}]^{22-}$ (ala = alanine), an inorganic cryptate $[Mn\{Ce_4As_4W_{41}O_{149}\}_2]^{46-}$,[25] and an interesting 3d–4f heterometallic AT trimer $[K\subset\{FeCe(AsW_{10}O_{38})(H_2O)_2\}_3]^{14-}$.[26] In 2013, Li and co-workers synthesized three 1D chain RECATs $[RE_6(H_2O)_x\{As_4W_{44}(OH)_2(proline)_2O_{151}\}]^{10-}$ (RE^{3+} = Tb^{3+}, Dy^{3+}, x = 22; RE^{3+} = Nd^{3+}, x = 26).[27] Wassermann and Pope discovered a family of supramolecular aggregate $[Ce_{16}(H_2O)_{36}(B\text{-}\alpha\text{-}AsW_9O_{33})_{12}(WO_2)_4(W_2O_6)_8(W_5CeO_{18})_4]^{76-}$ and $[(H_2O)_{11}RE(Ln_2OH)(B\text{-}\alpha\text{-}AsO_3W_9O_{30})_4(WO_2)_4]^{20-}$ (RE^{3+} = Ce^{3+}, Nd^{3+}, Sm^{3+}, and Gd^{3+}).[28,29] Fukaya and Yamase reported two alkali-metal-controlled crown-shaped RECAT rings $[K\{Eu(H_2O)_2(\alpha\text{-}AsW_9O_{33})\}_6]^{35-}$ and $[Cs\{Eu(H_2O)_2(\alpha\text{-}AsW_9O_{33})\}_4]^{23-}$.[30] Nadjo and co-workers and our laboratory reported multi-transition-metal (TM)-substituted ATs and studied their magnetic properties.[31–33] In 2012 and 2015, our group consequently investigated several types of TM–RE heterometallic AT.[34]

It is obvious that there are very few reports on amino acid-containing RECATs,[6,9,25] which provides us an excellent opportunity and a great possibility to explore this research realm further. Moreover, amino acid ligands with flexible carboxyl and amino coordination sites allow these ligands to utilize multifunctional coordination modes to combine various metal centers, thus giving rise to unique metal–oxo cluster aggregates with novel structures and interesting properties. Above all, the majority of the previously reported RECATs were prepared from AT precursors by using a stepwise synthetic strategy. However, the one-step self-assembly strategy with sodium tungstate, arsenic trioxide, amino acid ligands, and RE^{3+} ions under laboratory conditions to synthesize amino acid-containing RECAT aggregates has been seldom utilized, which is of great interest for us. In this one-step self-assembly process, it is not necessary to prepare AT precursors, which can drastically curtail the experimental procedures. It is well known that there are enormous possibilities and unpredictabilities in creating novel species derived from the combination of AT fragments generated in situ and RE ions with amino acid ligands during the course of a one-step self-assembly process. In this context, we have begun to employ this one-step self-assembly strategy to prepare neoteric organic–inorganic hybrid RECAT aggregates by using the synergistic effect of two types of organic solubilizer (i.e., dimethylamine hydrochloride and L-serine); however, reaction systems that include one of these organic solubilizers have been recently exploited by us in the discovery of two series of novel RECATs, such as $[H_2N(CH_3)_2]_6Na_{24}H_{16}\{[RE_{10}W_{16}(H_2O)_{30}O_{50}](B\text{-}\alpha\text{-}AsW_9O_{33})_8\}\cdot 97\,H_2O$ (RE^{3+} = Eu^{3+}, Sm^{3+}, Gd^{3+}, Tb^{3+}, Dy^{3+}, Ho^{3+}, Er^{3+}, and Tm^{3+}) and $[H_2N(CH_3)_2]_8Na_8\{[W_3RE_2(H_2O)_8AsO_8(OH)][B\text{-}\alpha\text{-}AsW_9O_{33}]_2\}_2\cdot 65\,H_2O$ (RE^{3+} = Eu^{3+}, Gd^{3+}, Tb^{3+}, Dy^{3+}, Ho^{3+}, and Y^{3+}).[35] In this reaction system, synergistic effects of the two organic solubilizers are present. One organic solubilizer (i.e., dimethylamine hydrochloride) can, to some degree, ameliorate the reactivity of sodium tungstate and arsenic trioxide with RE^{3+} ions in an aqueous acidic medium and effectively decrease the possibility of precipitation caused by the AT fragments generated in situ and RE^{3+} ions; furthermore, this organic solubilizer can simultaneously serve as the organic cation to balance the charge of the resulting products. Whereas the other solubilizer (i.e., L-serine) can function as a chelating functional ligand to induce the aggregation of different metal centers and thus construct novel RECAT aggregates. Furthermore, the synergetic effects of these two organic solubilizers can not only facilitate the formation and crystallization of the desired products, but also can stabilize the structures of the desired products.

Based on this strategy, we obtained three classes of Ser-decorated RECAT $[H_2N(CH_3)_2]_6NaH[RE_2W_4O_{10}(H_2O)_8(Ser)_2(B\text{-}\alpha\text{-}AsW_9O_{33})_2]\cdot 30\,H_2O$ (RE^{3+} = Eu^{3+}, Gd^{3+}, Tb^{3+}, Dy^{3+}, Ho^{3+}, Er^{3+}, Tm^{3+}, Yb^{3+}, and Y^{3+}; **1**), $[H_2N(CH_3)_2]_6Na_{6-x}RE_xH_{4-2x}[RE_4W_8O_{19}(H_2O)_{10+y}(OH)_2(Ser)_2(B\text{-}\alpha\text{-}AsW_9O_{33})_4]\cdot n\,H_2O$ (RE^{3+} = Tb^{3+}, x = 1, y = 2, n = 36; RE = Dy^{3+}, Ho^{3+}, Er^{3+}, Yb^{3+}, Y^{3+}, x = 0, y = 0, n = 38; RE^{3+} = Tm^{3+}, x = 1, y = 0, n = 38; **2**), and $[H_2N(CH_3)_2]_{6-2x}Na_{2+3x}RE_xH_{10-6x+y}[RE_4W_8O_{19}(H_2O)_8(OH)_2(Ser)_4(B\text{-}\alpha\text{-}AsW_9O_{33})_4]\cdot Cl_y\cdot n\,H_2O$ (RE^{3+} = Ce^{3+}, Pr^{3+}, x = 1, y = 0, n = 65; RE^{3+} = Nd^{3+}, Sm^{3+}, x = 0, y = 0, n = 65; RE^{3+} = Eu^{3+}, Gd^{3+}, x = 1, y = 2, n = 45; **3**). Type **1** reveals a Ser-decorated di-RE-substituted sandwich-type dimeric structure constructed from two trilacunary Keggin $[B\text{-}\alpha\text{-}AsW_9O_{33}]^{9-}$ fragments that sandwich a $[RE_2W_4O_{10}(H_2O)_8(Ser)_2]^{10+}$ core, whereas types **2** and **3** display the Ser-decorated tetra-RE-substituted tetrameric square assembly established by four trilacunary Keggin $[B\text{-}\alpha\text{-}AsW_9O_{33}]^{9-}$ fragments that encapsulate a central dual- or tetra-Ser-participating $[RE_4W_8O_{19}(H_2O)_{10+y}(OH)_2(Ser)_2]^{20+}$ or $[RE_4W_8O_{19}(H_2O)_8(OH)_2(Ser)_4]^{20+}$ core. Most interestingly, the use of different amounts of RE^{3+} salts leads to structural transformation from dimerization to tetramerization of Ser-decorated RECATs. Type **1** was obtained when 0.10 grams of $RE(NO_3)\cdot 6\,H_2O$ was used in the reaction, whereas type **2** and **3** were obtained when the amount of $RE(NO_3)\cdot 6\,H_2O$ used increased to 0.20 grams. Unexpectedly, the influence of the inherent nature of the RE^{3+} ions results in the structural discrepancy of types **2** and **3**. To the best of our knowledge, this structural transformation derived from the use of different amounts of RE^{3+} salts has scarcely been encountered in the field of POM chemistry.

The solid-state luminescent properties and lifetime–decay behaviors of **1-Eu**, **1-Tb**, **1-Dy**, **1-Ho**, **1-Er**, **1-Tm**, **2-Tb**, **2-Dy**, **2-Ho**, **2-Er**, **2-Tm**, **3-Pr**, **3-Nd**, **3-Sm**, and **3-Eu** have been investi-

gated. The chromaticity coordinates of **1-Eu**, **1-Tb**, **1-Dy**, **1-Ho**, **1-Er**, **1-Tm**, **2-Tb**, **2-Dy**, **2-Ho**, **2-Er**, **2-Tm**, **3-Pr**, **3-Sm**, and **3-Eu** have been indexed, and the dominant wavelengths, color purities, and correlated color temperatures have also been calculated for these compounds.

Results and Discussion

Synthesis

As part of our continuing work on one-step self-assembly strategies to prepare novel organic–inorganic hybrid RECAT aggregates, compounds **1**–**3** were prepared by treating $Na_2WO_4{\cdot}2H_2O$ and As_2O_3 with $RE(NO_3)_3{\cdot}6H_2O$ with the introduction of two organic solubilizers (i.e., dimethylamine hydrochloride and L-serine) under acidic conditions (see the Experimental Section in the Supporting Information). During the course of our investigation, we firstly used $RE(NO_3)_3{\cdot}6H_2O$ (0.100 g; RE^{3+} = Eu^{3+}, Gd^{3+}, Tb^{3+}, Dy^{3+}, Ho^{3+}, Er^{3+}, Tm^{3+}, Yb^{3+}, and Y^{3+}) to treat other simple materials, thus giving rise to type **1**. Considering the influence of the amount of RE^{3+} ions used, when we increased the quantity from 0.10 to 0.20 grams under the same conditions and, beyond our expectation, type **2** (RE^{3+} = Tb^{3+}, Dy^{3+}, Ho^{3+}, Er^{3+}, Tm^{3+}, Yb^{3+}, and Y^{3+}) was obtained. The results of parallel experiments reveal that different amounts of RE^{3+} ions may result in the various products, thus indicating that the amount of RE^{3+} ions is also an important factor in the reaction process. Type **2** could not be obtained when the amount of RE^{3+} ions varied from 0.10 to 0.05 grams, whereas type **1** was produced, even if the yield was very low. When the amount of RE^{3+} ions varied from 0.10 to 0.20 grams, mixed phases of **1** and **2** could be obtained. (The shapes of crystals of **1** (tetragonal prism crystals) and **2** (square block crystals) are different; therefore, the two types of crystal can be mechanically separated and identified by means of powder X-ray diffraction as shown in Figure S1 in the Supporting Information.) When the amount of RE^{3+} ions used changed from 0.20 to 0.25 grams, type **1** could not be harvested, whereas type **2** could still be separated. It is most interesting that when Ce^{3+}, Pr^{3+}, Nd^{3+}, or Sm^{3+} ions were used in the same synthetic method used to obtained type **1**, type **3** was isolated. When Eu^{3+} or Gd^{3+} ions were used in the same synthetic method used to obtain type **2**, type **3** was found (Scheme 1). According to the compositions of **1**–**3**, as determined by means of X-ray diffraction studies, the RE/W ratios are similar for the whole series, irrespective of which RE^{3+} ions were used; however, one can readily infer that the use of larger amounts of RE^{3+} ions produces compounds with larger RE/serine ratios (i.e., 1:1 for **1** and 2:1 for **2** and **3**). It is likely that the enhanced number of RE^{3+} ions in types **2** and **3**, and consequently the coordination sites available, makes these products more prone to extending their dimensionality.

In addition, the pH value is also a sensitive factor in the reaction and has an important effect on the crystallization and structural construction of the products. Our experimental investigations indicate that pH 2.3–3.0 is helpful for the formation of **1**–**3**, whereas their yields are the highest when the pH value is adjusted to pH 2.5, with the other conditions remaining unchanged. Furthermore, dimethylamine hydrochloride is considered to be indispensable and plays a significant role in improving the solubility of the RE^{3+} ions and ameliorating the reactivity of the RE^{3+} ions with sodium tungstate and arsenic trioxide. If dimethylamine hydrochloride is absent, the reaction system will gradually become turbid under stirring, lots of amorphous precipitation will be formed, and **1**–**3** will fail to be produced. On the contrary, when dimethylamine hydrochloride is present, the reaction system remains clear when stirred and **1**–**3** can be successfully obtained.

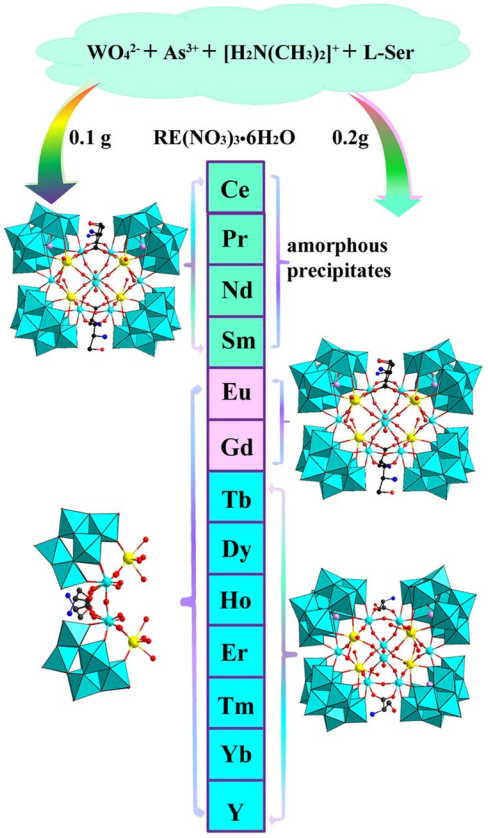

Scheme 1. The schematic synthetic processes of **1**–**3**.

In addition, single-crystal X-ray diffraction analyses illustrate that **1** crystallizes in the chiral monoclinic space group *C*2, whereas **2** and **3** crystallize in the achiral triclinic space group $P\bar{1}$, thus demonstrating that **1** is chiral and **2** and **3** are achiral. This outcome can be further confirmed by means of solid-state circular dichroism (CD) spectroscopic analysis of **1-Eu**, **2-Dy**, and **3-Ce** (Figure S2 in the Supporting Information). The CD spectrum of **1-Eu** shows a weak Cotton effect, whereas the CD spectra of **2-Dy** and **3-Ce** did not display the Cotton effect, thus showing that **1-Eu** is chiral and **2-Dy** and **3-Ce** are achiral. Furthermore, when we utilized D-serine to replace the L-serine ligand under the same conditions, analogues could also be isolated (Figure S3 in the Supporting Information). We will continue to explore the influence of chiral ligands on the structural variation and relevant properties of the resulting compounds.

Structure description

X-ray single-crystal diffraction studies show that type **1** crystallizes in the monoclinic space group *C*2 (Table S2 in the Supporting Information). The polyoxoanion of type **1** is a Ser-decorated di-RE^{3+}-substituted dimeric sandwich-type assembly in which a ship-shaped dual-Ser-participating $[RE_2W_4O_{10}(H_2O)_8(Ser)_2]^{10+}$ unit ($RE^{3+}=Eu^{3+}$, Gd^{3+}, Tb^{3+}, Dy^{3+}, Ho^{3+}, Er^{3+}, Tm^{3+}, Yb^{3+}, and Y^{3+}) connects two trivacant Keggin $[B\text{-}\alpha\text{-}AsW_9O_{33}]^{9-}$ fragments. In accordance with the effect of lanthanide contraction, the RE–O bond lengths decrease as the ionic radii of the RE^{3+} ions decrease. Therefore, only the structure of **1-Eu** is described as an example below. The molecular structure of **1-Eu** consists of a dimeric sandwich-type $[Eu_2W_4O_{10}(H_2O)_8(Ser)_2(B\text{-}\alpha\text{-}AsW_9O_{33})_2]^{8-}$ polyoxoanion (see Figure 1a and Figure S4a in the Supporting Information), a Na^+ ion, six monoprotonated $[H_2N(CH_3)_2]^+$ ions, a proton, and thirty lattice water molecules. Bond valence sum (BVS) calculations of **1-Eu** indicate that the oxidation states of the W, As, and Eu centers are +6, +3, and +3, respectively (Table S3 in the Supporting Information).[36] In the polyoxoanion, two trivacant Keggin $[B\text{-}\alpha\text{-}AsW_9O_{33}]^{9-}$ fragments are combined through two extraneous $[W_2O_5(Ser)]^{2+}$ groups, and two extraneous $[Eu(H_2O)_4]^{3+}$ ions each form a link to one $[B\text{-}\alpha\text{-}AsW_9O_{33}]^{9-}$ fragment and one $[W_2O_5(Ser)]^{2+}$ group through four terminal oxygen atoms. It is of extreme interest that the central cavity in the polyoxoanion encapsulates a Na^+ ion and forms $[NaEu_2W_4O_{10}(H_2O)_8(Ser)_2(B\text{-}\alpha\text{-}AsW_9O_{33})_2]^{7-}$ (Figure S5 in the Supporting Information) to enhance its structural stability. Notably, two W centers and one Eu center are situated at three vacant positions of a $[B\text{-}\alpha\text{-}AsW_9O_{33}]^{9-}$ fragment and form a Ser-decorated mono-Eu^{3+}-substituted hendecatungstate segment (see Figure 1b and Figure S4b in the Supporting Information). Two $[B\text{-}\alpha\text{-}AsW_9O_{33}]^{9-}$ fragments exhibit the well-known trivacant Keggin B-α-configuration derived from the removal of a $\{W_3O_{13}\}$ triad from the saturated α-Keggin structure and the W–O bond lengths vary from 1.702(12) to 2.423(11) Å, and the As···O distances are in the range 1.791(10)–1.810(11) Å (Figure 1c). In the dual-Ser-participating $[Eu_2W_4O_{10}(H_2O)_8(Ser)_2]^{10+}$ entity (Figure 1c), there is a crystallographically independent Eu^{3+} ion that exhibits a octa-coordinate distorted-square antiprismatic geometry (Figure S4c in the Supporting Information), which is defined by two μ_2-O atoms from two extraneous $\{WO_6\}$ octahedra (Eu–O: 2.376(11)–2.405(11) Å), two μ_2-O atoms from one $[B\text{-}\alpha\text{-}AsW_9O_{33}]^{9-}$ fragment (Eu–O: 2.367(12)–2.389(11) Å), and four coordinate water molecules (Eu–O: 2.440(12)–2.52113) Å). In addition, in the six-membered metal ring $[Eu_2W_4O_{10}(H_2O)_8(Ser)_2]^{10+}$ unit (Figure 1d), two crystallographically independent W atoms (i.e., W10 and W11) show a hexa-coordinate distorted-octahedral geometry that comprises two μ_2-O atoms from one $[B\text{-}\alpha\text{-}AsW_9O_{33}]^{9-}$ fragment (W–O: 1.917(11)–2.179(10) Å), one μ_2-O atom from another extraneous $\{WO_6\}$ octahedron (W–O: 1.905(9)–1.948(9) Å), one O atom from the Ser ligand (W–O: 2.191(10)–2.296(11) Å), one μ_2-O atom that connects the $Eu1^{3+}$ ion (W–O: 1.725(11)–1.748(11) Å), and one terminal O atom (W–O: 1.736(10)–1.748(11) Å). It is noteworthy that two amino acid-bridging $[W_2O_5(Ser)]^{2+}$ dimeric groups are observed in **1-Eu** and two $[W_2O_5(Ser)]^{2+}$ dimeric groups simultaneously form links to two trivacant Keggin $[B\text{-}\alpha\text{-}AsW_9O_{33}]^{9-}$ fragments. As far as we know, this phenomenon has not been observed in POM chemistry before. In the Ser-bridging $[W_2O_5(Ser)]^{2+}$ group, the Ser ligand (Figure 1e) acts as a chelating group to bridge two W centers. In the case of the $[Eu_2W_4O_{10}(H_2O)_8(Ser)_2]^{10+}$ unit, four W centers and two Eu centers are connected in an orderly manner and give rise to an intriguing boat configuration if all the oxygen atoms, water ligands, and Ser ligands are omitted (Figure 1f).

Alternatively, the dimeric $[Eu_2W_4O_{10}(H_2O)_8(Ser)_2(B\text{-}\alpha\text{-}AsW_9O_{33})_2]^{8-}$ polyoxoanion can be written as $[Eu(H_2O)_4(Ser)(AsW_{11}O_{38})]_2^{8-}$, which can be assumed to be a combination of two mono-Eu^{3+} incorporated $[Eu(H_2O)_4(Ser)(AsW_{11}O_{38})]^{4-}$ half-units (see Figure 1b and Figure S6a in the Supporting Information) through two μ_2-O atoms and two Ser ligands. It should be pointed out that the mono-Eu^{3+}-incorporated $[Eu(H_2O)_4(Ser)(AsW_{11}O_{38})]^{4-}$ half-unit somewhat resembles the $[(AsW_{11}O_{39})\{Re(CO)_3\}_3(\mu_3\text{-}OH)(\mu_2\text{-}OH)]^{6-}$ cluster (Figure S6b in the Supporting Information) reported by Niu and co-workers.[13] Nonetheless, the $[As^{III}W_{11}O_{41}]^{13-}$ subunit (Figure S6c in the Supporting Information) in the $[Eu(H_2O)_4(Ser)(AsW_{11}O_{38})]^{4-}$ half-unit is remarkably different from the classical monovacant Keggin $[As^{V}W_{11}O_{39}]^{7-}$ subunit (Fig-

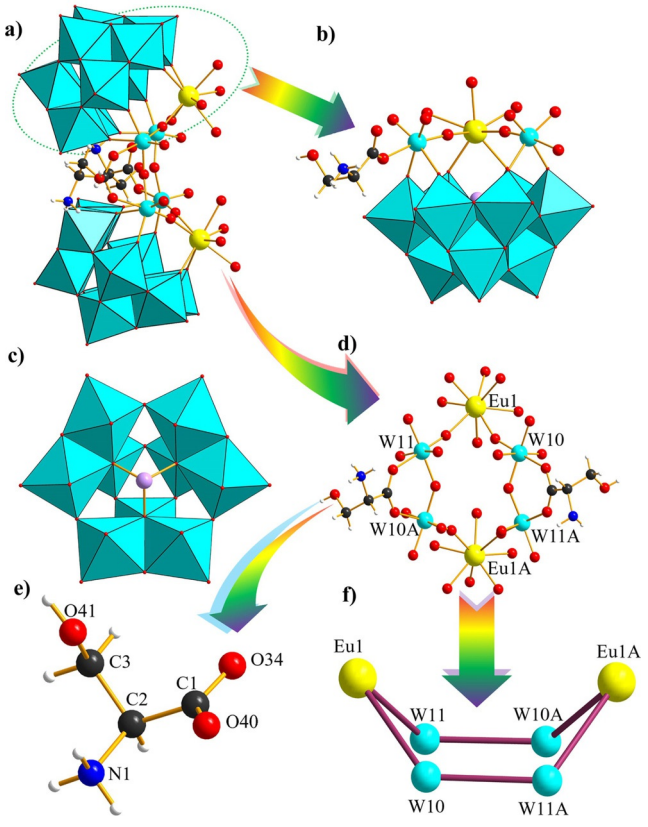

Figure 1. a) The dimeric sandwich-type polyoxoanion of **1-Eu**. b) The Ser-decorated mono-Eu^{III}-substituted hendecatungstate segment in **1-Eu**. c) The $[B\text{-}\alpha\text{-}AsW_9O_{33}]^{9-}$ fragment. d) The six-membered metal ring $[Eu_2W_4O_{10}(H_2O)_8(Ser)_2]^{10+}$ unit in **1-Eu**. e) The structure of the Ser ligand. f) The simplified connective mode of the $[Eu_2W_4O_{10}(H_2O)_8(Ser)_2]^{10+}$ unit that displays a boat configuration. Symmetry code: A: 1−*x*, *y*, 1−*z*.

ure S6d in the Supporting Information) in the $[(As\text{-}W_{11}O_{39})\{Re(CO)_3\}_3(\mu_3\text{-}OH)(\mu_2\text{-}OH)]^{6-}$ cluster. The $[As^{III}W_{11}O_{41}]^{13-}$ subunit is considered to comprise two additional $\{WO_6\}$ octahedra that graft to the lacunary sites of a trivacant Keggin [B-α- $As^{III}W_9O_{33}]^{9-}$ fragment, in which each $\{WO_6\}$ octahedron is connected to two lacunary oxygen atoms from a [B-α-$As^{III}W_9O_{33}]^{9-}$ fragment; however, these two $\{WO_6\}$ octahedra are not linked to each other. Such a $[As^{III}W_{11}O_{41}]^{13-}$ subunit has been encountered in our studies.[35]

When the amount of $RE(NO_3)\cdot 6H_2O$ ($RE^{3+}=Tb^{3+}$, Dy^{3+}, Ho^{3+}, Er^{3+}, Tm^{3+}, Yb^{3+}, and Y^{3+}) was increased to 0.20 grams, type **2** was unexpectedly isolated. Unlike type **1**, type **2** crystallizes in the triclinic space group $P\bar{1}$. Although there are some differences in the countercations on the periphery of the polyoxoanions, the main polyoxoanion skeleton of type **2** illustrates a dual-Ser-decorated tetra-RE^{3+}-incorporated tetrameric square structure established by four [B-α-$AsW_9O_{33}]^{9-}$ fragments that anchor a central dual-Ser-participating $[RE_4W_8O_{19}(H_2O)_{10}(OH)_2(Ser)_2]^{20+}$ core; as a result, only the structure of **2-Dy** is described herein. The tetrameric square polyoxoanion of **2-Dy** (see Figure 2a and Figure S7 in the Supporting Information) is constructed from a fascinating dodenuclear heterometallic $[Dy_4W_8O_{19}(H_2O)_{10}(OH)_2(Ser)_2]^{20+}$ core (Figure 2b) in the center of a square that joins four trivacant Keggin [B-α-$AsW_9O_{33}]^{9-}$ fragments (Figure 2e) on four vertexes of the square through 24 μ_2-O atoms from four [B-α-$AsW_9O_{33}]^{9-}$ fragments. BVS calculations of **2-Dy** indicate that the oxidation states of the W, As, and Dy centers are +6, +3, and +3, respectively (Table S4 in the Supporting Information).[36] In the polyoxoanion, two [B-α-$AsW_9O_{33}]^{9-}$ fragments on a pair of the parallel edges of the square are bridged by a dimeric $[W_2O_5(Ser)]^{2+}$ group through four μ_2-O atoms, whereas two [B-α-$AsW_9O_{33}]^{9-}$ fragments on the other pair of the parallel edges of the square are connected by a monomeric $[WO_2]^{2+}$ group of four μ_2-O atoms. Attractively, a dimeric $[W_2O_5(OH)_2]$ segment joins two dimeric $[W_2O_5(Ser)]^{2+}$ groups through four μ_2-O atoms, whereas two $[Dy(H_2O)_3]^{3+}$ ions and two $[Dy(H_2O)_2]^{3+}$ ions connect two $[W_2O_5(Ser)]^{2+}$ groups, two $[WO_2]^{2+}$ groups, and the $[W_2O_5(OH)_2]$ segment . To our knowledge, this connective mode is the first to be observed. The heterometallic $[Dy_4W_8O_{19}(H_2O)_{10}(OH)_2(Ser)_2]^{20+}$ core (Figure 2b) is constituted by two $[Dy(H_2O)_3]^{3+}$ ions, two $[Dy(H_2O)_2]^{3+}$ ions, two $[W_2O_5(Ser)]^{2+}$ groups, and one $[W_2O_5(OH)_2]$ segment. Two $[W_2O_5(Ser)]^{2+}$ groups are combined with the $[W_2O_5(OH)_2]$ segment in a perpendicular fashion, thus generating a hexatungstate $[W_6O_{15}(OH)_2(Ser)_2]^{2+}$ group; alternatively, this groups can be seen as a fusion of two trinuclear $[W_3O_7(OH)(Ser)]^{3+}$ clusters by sharing an oxygen atom (i.e., O79; Figure 2c).

Moreover, this hexatungstate $[W_6O_{15}(OH)_2(Ser)_2]^{2+}$ group is further stabilized by two $[Dy(H_2O)_3]^{3+}$ ions and two $[Dy(H_2O)_2]^{3+}$ ions on both sides. In the heterometallic $[Dy_4W_8O_{19}(H_2O)_{10}(OH)_2(Ser)_2]^{20+}$ core, the W1 and W2 centers are linked by a chelating Ser ligand and a μ_2-O atom; furthermore, four Dy^{3+} ions (i.e., Dy1, Dy2, Dy1A, and Dy2A) are aligned in a rectangle that is 6.7733×6.3347 Å in size and four W centers (i.e., W22, W3, W22A, and W3A) are arranged in a parallelogram that is 5.9978×5.6763 Å in size (Figure 2d). It is worth noting that the crystallographically independent $Dy1^{3+}$ ion resides in an octa-coordinate distorted-square antiprismatic geometry defined by three μ_2-O atoms from three $\{WO_6\}$ octahedra (i.e., W2, W3, and W22A; Dy–O: 2.316(16)–2.353(19) Å), two μ_2-O atoms from one [B-α-$AsW_9O_{33}]^{9-}$ fragment (Dy–O: 2.301(19)–2.324(16) Å), and three coordinated water molecules (Dy–O: 2.40(3)–2.48(3) Å; see Figure S8a in the Supporting Information). The hepta-coordinate monocapped trigonal-prism geometry of the $Dy2^{3+}$ ion constitutes three μ_2-O atoms from three $\{WO_6\}$ octahedra (i.e., W1A, W3, and W22; Dy–O: 2.260(14)–2.332(17) Å), two μ_2-O atoms from one [B-α-$AsW_9O_{33}]^{9-}$ fragment (Dy–O: 2.300(16)–2.371(15) Å), and two terminal coordinate water molecules (Dy–O: 2.29(2)–2.426(18) Å; see Figure S8b in the Supporting Information). At the first glimpse, the polyoxoanion of **2-Dy** is somewhat similar to the previously reported RECAT $[Ce^{III}_2(OH)_2(WO_2)_4(H_2O)_{10}(B\text{-}\alpha\text{-}AsW_9O_{33})_4(WO_2)_4]^{18-}$ (Figure 2f) reported by Wassermann and Pope.[29] However, it is not difficult to observe some significant differences between these compounds, although both contain four trivacant Keggin [B-α-$AsW_9O_{33}]^{9-}$ fragments: 1) The former (i.e., **2-Dy**) is an amino acid-involving organic–inorganic hybrid cluster, whereas the latter (i.e., $[Ce^{III}_2(OH)_2(WO_2)_4(H_2O)_{10}(B\text{-}\alpha\text{-}AsW_9O_{33})_4(WO_2)_4]^{18-}$) is an inorganic cluster; 2) the former includes a dodenuclear heterometallic $[Dy_4W_8O_{19}(H_2O)_{10}(OH)_2(Ser)_2]^{20+}$ core and the latter consists of an octa-nuclear heterometallic $[Ce_4(OH)_2(H_2O)_{10}W_4O_8]^{18+}$ core (Figure 2g); 3) four trivacant Keggin fragments constitute a rectangle in the former, whereas four trivacant Keggin fragments stand on the four vertexes of a distorted tetrahedron in the latter; 4) the former contains four Dy^{3+} ions that are distributed in a rectangle, in which two Dy^{3+} ions are octa-coordinate and the other two Dy^{3+} ions are hepta-coordinate, in the contrast, the latter contains four Ce^{3+} ions that are arranged in a tetrahedron (Figure 2h) and show an octa-coordinate geometry.

From another perspective, the polyoxoanionic skeleton of **2-Dy** (Figure 3a) can be described as two lacunary $[As_2W_{19}O_{68}]^{16-}$ units (Figures 3b,d) that sandwich a heterometallic $[Dy_4W_6O_{15}(OH)_2(H_2O)_{10}(Ser)_2]^{16+}$ cluster (Figure 3c), in which the Z-shaped hexatungstate $[W_6O_{15}(OH)_2(Ser)_2]^{2+}$ group is seen (Figure 3e). It is worth mentioning that the lacunary $[As_2W_{19}O_{68}]^{16-}$ unit (Figure S9a in the Supporting Information) in **2-Dy** is analogous to the $[As_2W_{19}O_{67}(H_2O)]^{14-}$ precursor (Figure S9b in the Supporting Information) found by Tourné et al. in 1973,[37a] and its structure was determined by Kortz et al. in 2001.[37b]

In addition, careful observation shows that **2-Tb** is somewhat disparate from **2-Dy**, although **2-Tb** and **2-Dy** are very similar in structure. The most remarkable difference is that the $Tb1^{3+}$ and $Tb2^{3+}$ ions exhibit an octa-coordinate distorted-square antiprism geometry (see Figure 4a and Figure S10 in the Supporting Information), whereas the $Dy1^{3+}$ ion shows an octa-coordinate distorted-square antiprism geometry and the $Dy2^{3+}$ ion exhibits a hepta-coordinate distorted monocapped trigonal-prism geometry (see Figures 4b and Figure S8 in the Supporting Information). This difference may be primarily derived from the effect of lanthanide contraction.

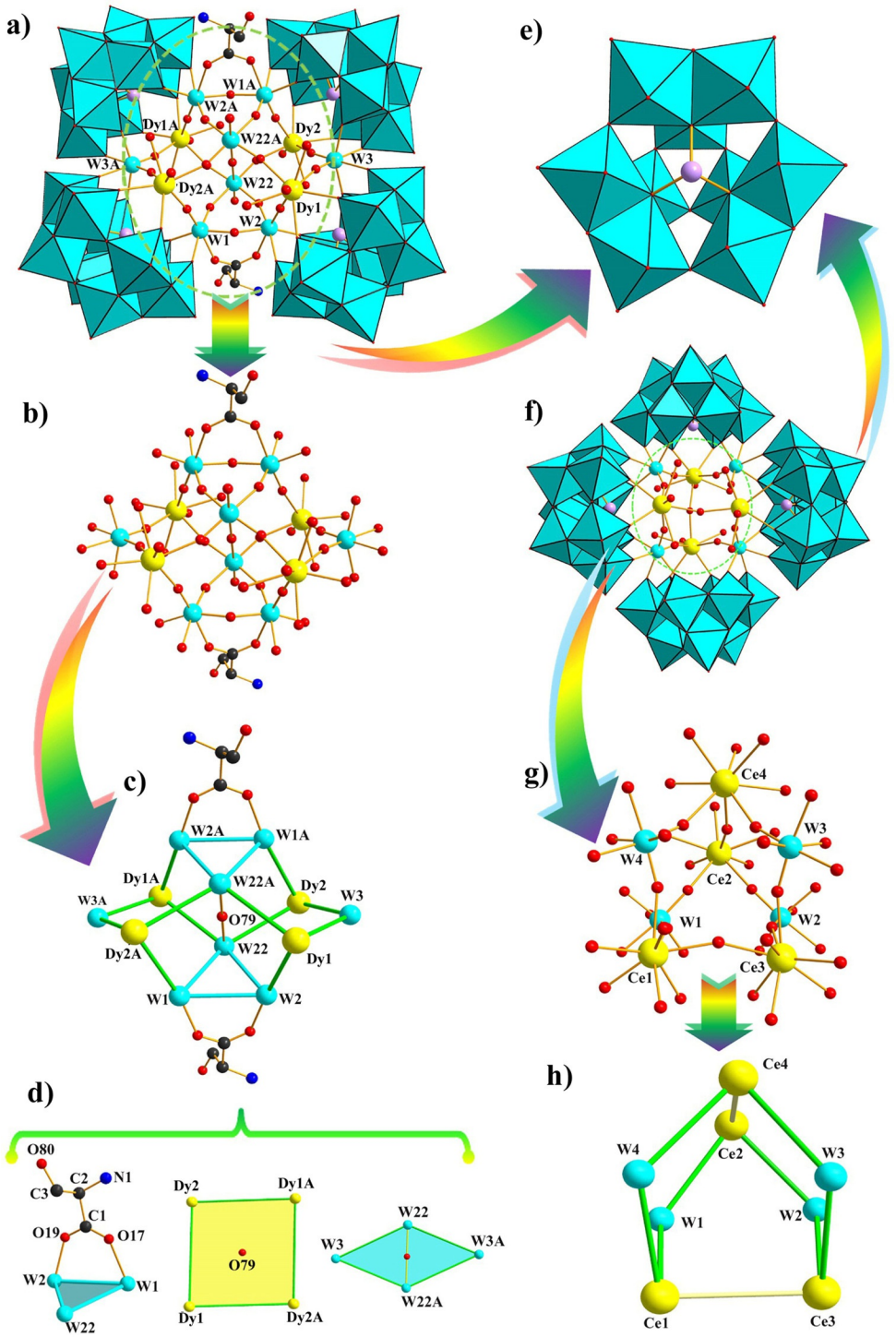

Figure 2. a) The tetrameric square polyoxoanion of **2-Dy** with a selected numbering scheme. b) The fascinating dodenuclear $[Dy_4W_8O_{19}(H_2O)_{10}(OH)_2(Ser)_2]^{20+}$ core in **2-Dy**. c) The simplified connective mode of the $[Dy_4W_8O_{19}(H_2O)_{10}(OH)_2(Ser)_2]^{20+}$ core in **2-Dy**. d) The distribution geometry of the metal atoms. e) The $[B\text{-}\alpha\text{-}AsW_9O_{33}]^{9-}$ fragment in **2-Dy** and $[Ce^{III}_2(OH)_2(H_2O)_{10}(B\text{-}\alpha\text{-}AsW_9O_{33})_4(WO_2)_4]^{18-}$. f) The structure of $[Ce^{III}_2(OH)_2(H_2O)_{10}(B\text{-}\alpha\text{-}AsW_9O_{33})_4(WO_2)_4]^{18-}$. g) The octa nuclear $[Ce_4(OH)_2(H_2O)_{10}W_4O_8]^{18+}$ cluster in $[Ce^{III}_2(OH)_2(H_2O)_{10}(B\text{-}\alpha\text{-}AsW_9O_{33})_4(WO_2)_4]^{18-}$. h) The simplified connective mode of the $[Ce_4(OH)_2(H_2O)_{10}W_4O_8]^{18+}$ cluster. Symmetry code: A: $3-x$, $2-y$, $-2-z$.

Type **3** was isolated when the same synthetic method used to obtain type **1** and Ce^{3+}, Pr^{3+}, Nd^{3+}, and Sm^{3+} ions were used, and **3-Eu** and **3-Gd** were obtained when the same synthetic method used to obtain type **2** and Eu^{3+} and Gd^{3+} ions, respectively, were used. Type **3** belongs to the triclinic space group $P\bar{1}$. The polyoxoanion of type **3** is a tetra-Ser-decorated tetra-RE^{3+}-incorporated tetrameric square structure $[RE_4(H_2O)_8W_8(Ser)_4O_{19}(OH)_2(B\text{-}\alpha\text{-}AsW_9O_{33})_4]^{16-}$ established by four $[B\text{-}\alpha\text{-}AsW_9O_{33}]^{9-}$ fragments that embed a central tetra-Ser-participating $[RE_4W_8O_{19}(H_2O)_8(OH)_2(Ser)_4]^{20+}$ core. Therefore,

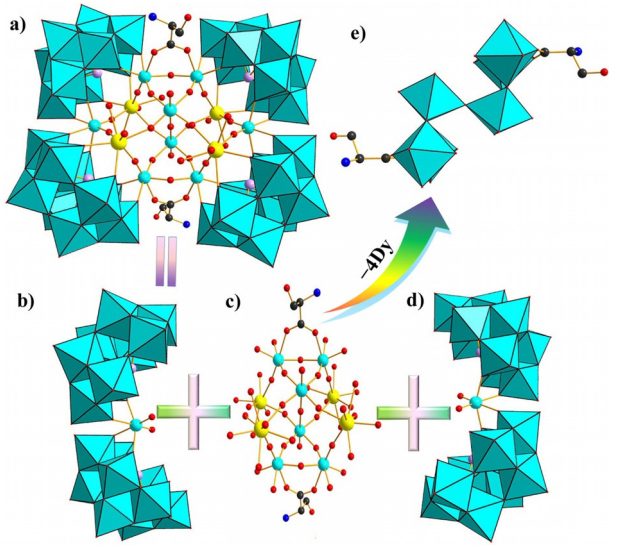

Figure 3. a) The polyoxoanion of **2-Dy**. b, d) The lacunary $[As_2W_{19}O_{68}]^{16-}$ fragment in **2-Dy**. c) The heterometallic $[Dy_4W_6O_{15}(OH)_2(H_2O)_{10}(Ser)_2]^{16+}$ cluster in **2-Dy**. e) The Z-shaped hexanuclear hybrid isopolyoxotungstate $[W_6O_{15}(OH)_2(Ser)_2]^{2+}$ group.

only the structure of **3-Ce** is described in detail. The polyoxoanionic skeleton of **3-Ce** (Figure 5a) is constructed from a tetra-Ser-participating dodenuclear $[Ce_4W_8O_{19}(H_2O)_8(OH)_2(Ser)_4]^{20+}$ core (Figure 5b) that links four trivacant Keggin $[B\text{-}\alpha\text{-}AsW_9O_{33}]^{9-}$ fragments. It should be pointed out that the dodenuclear $[Ce_4W_8O_{19}(H_2O)_8(OH)_2(Ser)_4]^{20+}$ cluster in **3-Ce** resembles the dodenuclear $[Tb_4W_8O_{19}(H_2O)_{12}(OH)_2(Ser)_2]^{20+}$ core in **2-Tb** very closely (Figure 4a). The structure of the dodenuclear $[Ce_4W_8O_{19}(H_2O)_8(OH)_2(Ser)_4]^{20+}$ cluster in **3-Ce** can be imagined to contain four carboxylic O atoms from two extraneous Ser ligands that substitute four water ligands on four Tb^{3+} ions in **2-Tb** and gives rise to the polyoxoanionic skeleton of type **3-Ce**, in which two pairs of neighboring Ce^{3+} ions are bridged by Ser ligands (Figure 5c). It is of particular concern that Ser ligands can only not join two Ce^{3+} ions together, but also can connect two W centers. As far as we know, this connective mode is unprecedented in coordination chemistry. In **3-Ce**, two crystallographically unique Ce^{3+} ions are embedded in the severely distorted-square antiprism geometry (Figure S11 in the Supporting Information).

In addition, the supramolecular packing representations of **1-Eu**, **2-Dy**, and **3-Ce** and related descriptions are given in the Supporting Information (Figures S12–S14).

Photoluminescence (PL) properties

The PL behaviors of RE-based materials have attracted considerable interest due to technological applications in lighting and displays, biomarkers, drug carriers, photovoltaic devices (e.g., tunable lasers, light-emitting diodes, amplifiers for optical communications, and optical storage), and so forth.[38] From the early discovery of lighting at the end of the 19th century, the invention of the bright-red-emitting phosphor Y_2O_3: Eu^{3+} at the beginning of the 20th century, and the appearance of the YAG: Nd^{3+} laser in 1964,[39] to date, some metal oxide luminescent materials, such as $BaMgAl_{10}O_{17}$: Eu^{2+} and $GdMgB_5O_{10}$: Ce^{3+},Tb^{3+} have been commercially used to manufacture blue and green luminescent lamps, respectively.[40] In principle, RE-based luminescent materials have aroused extensive interest because of the narrow emission line and high color purity derived from transitions inside the 4f shell of the RE^{3+} ions.[41–42] The 4f shells are located inside the completely filled 5s and 5p subshells. These outer completed shells protect the 4f electrons from active interactions with the environment and diminish the considerable influence of surrounding ions on the inner

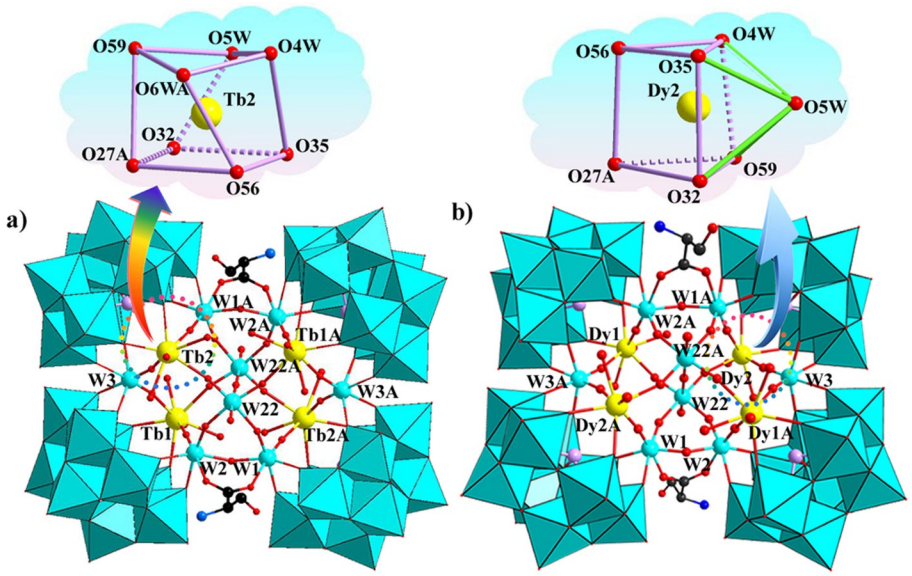

Figure 4. a) The polyoxoanion of **2-Tb** featuring the octa-coordinate distorted-square antiprism geometry of the $Tb2^{3+}$ ion. b) The polyoxoanion of **2-Dy** featuring the hepta-coordinate distorted monocapped triangular prism geometry of the $Dy2^{3+}$ ion.

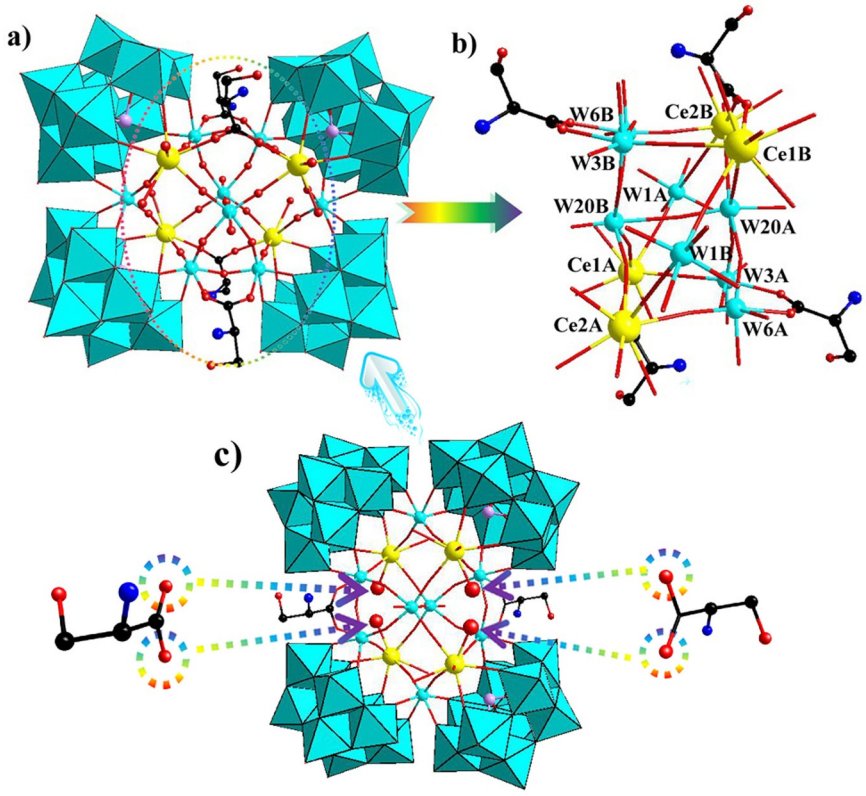

Figure 5. a) The tetrameric square polyoxoanion of **3-Ce**. b) The twelve-nuclear $[Ce_4(H_2O)_8W_8(Ser)_4O_{19}(OH)_2]^{20+}$ cluster in **3-Ce**. c) The tetrameric square polyoxoanion of **3-Ce** that highlights four coordinated water ligands from four Tb^{3+} ions that can be substituted by four carboxylic oxygen atoms from two extraneous Ser ligands. Symmetry code: A: $1+x$, $-1+y$, $-1+z$; B: $-1-x$, $-y$, $1-z$.

f orbitals. As a consequence, except for the La^{3+} and Lu^{3+} ions, each RE^{3+} ion shows narrow characteristic intra 4f–4f transitions. Therefore, the PL properties and lifetime–decay behaviors of the solid-state samples for **1-Eu**, **1-Tb**, **1-Dy**, **1-Ho**, **1-Er**, **1-Tm**, **2-Tb**, **2-Dy**, **2-Ho**, **2-Er**, **2-Tm**, **3-Pr**, **3-Nd**, and **3-Sm** have been investigated at room temperature (see Figures 6–9 and Figures S15–S21 in the Supporting Information), and the decay lifetimes and pre-exponential factors of these compounds are summarized in Tables S5 and S6 in the Supporting information. When **1-Eu** was excited under an ultraviolet light of $\lambda = 394$ nm, the emission spectrum was recorded between $\lambda = 500$ and 750 nm (Figure 6a), in which three weak and five obvious characteristic emission bands at $\lambda = 526$, 537, 554, 579, 594, 614, 650, and 701 nm are attributed to the $^5D_1 \rightarrow {}^7F_0$, $^5D_1 \rightarrow {}^7F_1$, $^5D_1 \rightarrow {}^7F_2$, $^5D_0 \rightarrow {}^7F_0$, $^5D_0 \rightarrow {}^7F_1$, $^5D_0 \rightarrow {}^7F_2$, $^5D_0 \rightarrow {}^7F_3$, and $^5D_0 \rightarrow {}^7F_4$ transitions, respectively, of the Eu^{3+} ion.[43] The red emission at $\lambda = 614$ nm from the $^5D_0 \rightarrow {}^7F_2$ transition was the most prominent. The symmetry-forbidden $^5D_0 \rightarrow {}^7F_0$ emission at $\lambda = 579$ nm is seen distinctly, which shows that the Eu^{3+} ion in **1-Eu** inhabits in low-symmetrical coordination environment.[40] It is worth noting that the $^5D_0 \rightarrow {}^7F_1$ emission is a magnetic-dipole (MD) transition and the $^5D_0 \rightarrow {}^7F_2$ emission is an electric-dipole (ED) transition. The intensity of the $^5D_0 \rightarrow {}^7F_2$ transition increases as the site symmetry of the Eu^{3+} ion decreases. As a consequence, the $I(^5D_0 \rightarrow {}^7F_2)/I(^5D_0 \rightarrow {}^7F_1)$ intensity ratio often behaves as a criterion for examining the local symmetry of the Eu^{3+} ion.[44] For **1-Eu**, the $I(^5D_0 \rightarrow {}^7F_2)/I(^5D_0 \rightarrow {}^7F_1)$ intensity ratio is approximately 6.6:1, further demonstrating the low-symmetrical coordination environment of the Eu^{3+} ion. This verdict is in good agreement with the case that the crystallographically independent Eu^{3+} ion in **1-Eu** exhibits an octa-coordinate distorted-square antiprism geometry. By monitoring the most intense emission at $\lambda = 614$ nm, the excitation spectrum of **1-Eu** was recorded (Figure S15a in the Supporting Information), which shows five peaks between $\lambda = 300$ and 500 nm, in which a narrow band at $\lambda = 394$ nm from the $^7F_0 \rightarrow {}^5L_6$ transition is the strongest and there are four remaining bands at $\lambda = 362$, 384, 415, and 465 nm that involve in the intra-4f transitions from the $^7F_0$ ground state to higher energy levels (^5D_J, ^5L_J, ^5G_J) of the Eu^{3+} ion.[43a,45] The decay curve of this transition on monitoring the more intense emission at $\lambda = 614$ nm can be fitted with a monoexponential function $I = A_{exp}(-t/\tau)$ (τ = lifetime and A = pre-exponential factor), thus affording $\tau = 227.15$ μs and $A = 6966.83$ (Figure 6b). In addition, irradiation with a UV lamp at $\lambda = 365$ nm results in the luminescence photograph of **1-Eu** that exhibits red light (Figure S16a in the Supporting Information). The solid-state sample of **1-Tb** emits green luminescence upon excitation at $\lambda = 378$ nm. Its emission spectrum displays four obvious and three weak characteristic emission peaks at $\lambda = 489$, 544, 584, 621, 647, 667, and 679 nm (Figure 6c), which correspond to the $^5D_4 \rightarrow {}^7F_6$, $^5D_4 \rightarrow {}^7F_5$, $^5D_4 \rightarrow {}^7F_4$, $^5D_4 \rightarrow {}^7F_3$, $^5D_4 \rightarrow {}^7F_2$, $^5D_4 \rightarrow {}^7F_1$, and $^5D_4 \rightarrow {}^7F_0$ transitions, respectively, of the Tb^{3+} ion.[46] Furthermore, by monitoring the most intense emission at $\lambda = 544$ nm, the excitation spectrum of **1-Tb** was obtained

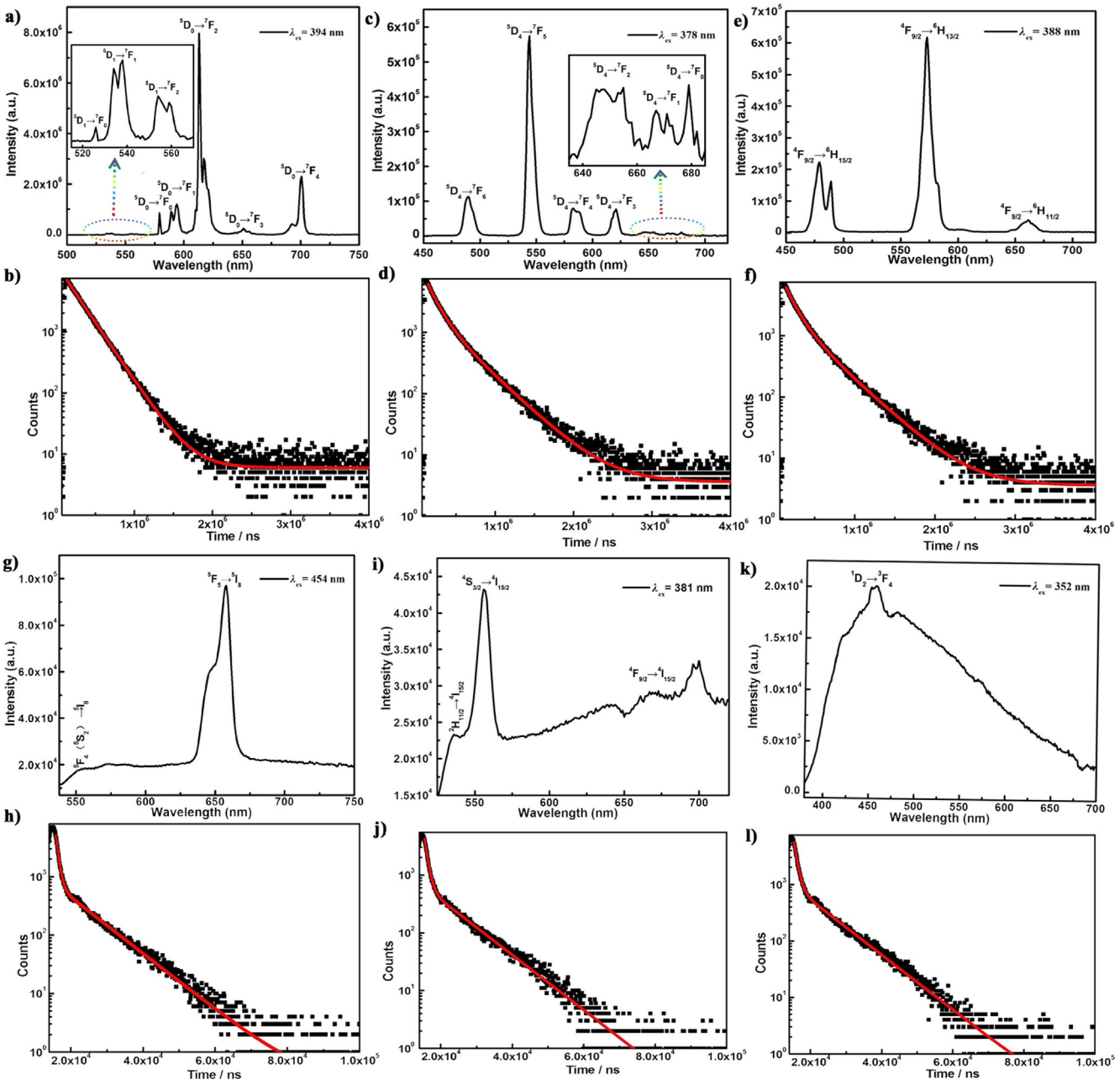

Figure 6. a) The PL emission spectrum of **1-Eu**. b) The lifetime decay curve of **1-Eu** obtained by monitoring the emission at $\lambda = 614$ nm. c) The PL emission spectrum of **1-Tb**. d) The lifetime-decay curve of **1-Tb** obtained by monitoring the emission at $\lambda = 544$ nm. e) The PL emission spectrum of **1-Dy**. f) The lifetime-decay curve of **1-Dy** obtained by monitoring the emission at $\lambda = 544$ nm. g) The PL emission spectrum of **1-Ho**. h) The lifetime-decay curve of **1-Ho** obtained by monitoring the emission at $\lambda = 660$ nm. i) The PL emission spectra of **1-Er**. j) The lifetime-decay curve of **1-Er** obtained by monitoring the emission at $\lambda = 556$ nm. k) The PL emission spectrum of **1-Tm**. l) The lifetime-decay curve of **1-Tm** obtained by monitoring the emission at $\lambda = 452$ nm.

and mainly consists of three characteristic bands centered at $\lambda = 342$, 359, and 378 nm (Figure S15b in the Supporting Information), which could be referred to the transitions from the $^7F_6$ ground state to the excited states of the $^5L_6$, $^5L_9$, and $^5G_6$ levels.[47] For **1-Tb**, the decay curve obtained on monitoring the more intense emission at $\lambda = 544$ nm (Figure 6d) was well fitted with a second-order exponential function $I = A_1\exp(-t/\tau_1) + A_2\exp(-t/\tau_2)$ (where τ_1 and τ_2 = fast and slow components of the luminescence lifetimes, respectively, and A_1 and A_2 = pre-exponential factors). The fitting lifetimes are $\tau_1 = 127.23$ μs (41.58%) and $\tau_2 = 361.50$ μs (58.42%) and the pre-exponential factors are $A_1 = 4135.58$ and $A_2 = 2044.76$. Therefore, the average decay time (τ^*) can be determined by using the formula $\tau^* = (A_1\tau_1^2 + A_2\tau_2^2)/(A_1\tau_1 + A_2\tau_2)$, thus the average lifetime is calculated to be 264.08 μs.[48] The luminescence photograph of **1-Tb** under the irradiation of a UV lamp at $\lambda = 365$ nm is shown in Figure S16b (see the Supporting information). When a solid-state sample of **1-Dy** was excited under an ultraviolet light of $\lambda = 388$ nm, the emission spectrum (Figure 6e) displays three characteristic peaks ascribed to the f–f transitions of the Dy^{3+}

ion, namely, the MD transition ($^4F_{9/2}\rightarrow{}^6H_{15/2}$) at $\lambda=478$ nm, the ED transition ($^4F_{9/2}\rightarrow{}^6H_{13/2}$) at $\lambda=574$ nm, and a weak emission band ($^4F_{9/2}\rightarrow{}^6H_{11/2}$) at $\lambda=662$ nm. The MD transition ($^4F_{9/2}\rightarrow{}^6H_{15/2}$) hardly varies with the coordination environment around the Dy^{3+} ion, whereas the ED $^4F_{9/2}\rightarrow{}^6H_{13/2}$ transition is strongly influenced by the chemical environment around the Dy^{3+} ion in the lattice. When the Dy^{3+} ion inhabits a low-symmetrical coordination environment, the emission that results from the $^4F_{9/2}\rightarrow{}^6H_{13/2}$ transition is often prominent in the emission spectrum. According to the spectrum of **1-Dy**, the intensity of the $^4F_{9/2}\rightarrow{}^6H_{13/2}$ transition is much higher than that of the $^4F_{9/2}\rightarrow{}^6H_{15/2}$ transition, thus implying that the Dy^{3+} ion occupies the lattice site without inversion symmetry.[49] This outcome is in good agreement with the octa-coordinate square antiprism geometry of the Dy^{3+} ion. By monitoring the emission at $\lambda=544$ nm, the excitation spectrum of **1-Dy** was obtained (Figure S15c in the Supporting Information) and includes four sharp peaks at $\lambda=352$, 366, 388, and 427 nm, which are assigned to the transitions of the Dy^{3+} ion from the ground $^6H_{15/2}$ to the higher energy levels of $^6P_{7/2}$, $^6P_{5/2}$, $^4I_{13/2}$, and $^4G_{11/2}$, respectively. The decay–time curve of **1-Dy** was monitored under the most intense emission at $\lambda=574$ nm (Figure 6f), which can be well fitted with a second-order exponential function. The fitting lifetimes were $\tau_1=6.04$ μs (28.18%) and $\tau_2=9.07$ μs (71.82%) and the average lifetime was calculated to be $\tau^*=8.21$ μs. Notably, the lifetime–decay behavior of **1-Dy** resembles $[H_2N(CH_3)_2]_6$ $Na_{24}H_{16}\{[Dy_{10}W_{16}(H_2O)_{30}O_{50}](B\text{-}\alpha\text{-}AsW_9O_{33})_8\}\cdot 97H_2O$,[35a] and $[H_2N(CH_3)_2]_8Na_8\{[W_3Dy_2(H_2O)_8AsO_8(OH)][B\text{-}\alpha\text{-}AsW_9O_{33}]_2\}_2\cdot 65H_2O$.[35b] The decay–time curves of these three RECATs all abide by a second-order exponential function and the AT fragments in their skeletons make a remarkable contribution to the lifetimes. The solid-state sample of **1-Ho** emits orange luminescence under excitation at $\lambda=454$ nm. The emission spectrum between $\lambda=500$ and 750 nm displays two characteristic emission bands at $\lambda=550$ and 660 nm (Figure 6g) that are attributed to the $^5F_4+{}^5S_2\rightarrow{}^5I_8$ and $^5F_5\rightarrow{}^5I_8$ transitions of the Ho^{3+} ion, respectively. The excitation spectrum of **1-Ho** obtained by monitoring the emission at $\lambda=660$ nm consists of three characteristic excitation peaks at $\lambda=418$, 454, and 485 nm (Figure S15d in the Supporting Information), which are assigned to the transitions of $^5I_8\rightarrow{}^5G_5$, $^5I_8\rightarrow{}^5G_6$, and $^5I_8\rightarrow{}^5F_3$, respectively, of the Ho^{3+} ion.[50] The decay–time curve of **1-Ho** on monitoring the emission at $\lambda=660$ nm (Figure 6h) conforms to a second-order exponential function, thus leading to $\tau_1=0.75$ μs (36.32%), $\tau_2=9.01$ μs (63.68%), and $\tau^*=6.01$ μs. When **1-Er** was excited under a light of $\lambda=381$ nm, the yellowish green luminescence was observed with three characteristic emission peaks at $\lambda=536$, 556, and 668 nm in the PL spectrum that are assigned to the $^2H_{11/2}\rightarrow{}^4I_{15/2}$, $^4S_{3/2}\rightarrow{}^4I_{15/2}$, and $^4F_{9/2}\rightarrow{}^4I_{15/2}$ transitions, respectively, of the Er^{3+} ion (Figure 6i). By monitoring the $^4S_{3/2}\rightarrow{}^4I_{15/2}$ emission at $\lambda=556$ nm, the excitation spectrum of **1-Er** was collected and displays three groups of excitation bands at $\lambda=365$, 381, and 408 nm, which are attributed to the $^4I_{15/2}\rightarrow{}^4G_{9/2}$, $^4I_{15/2}\rightarrow{}^4G_{11/2}$, and $^4I_{15/2}\rightarrow{}^2H_{9/2}$ transitions, respectively, of the Er^{3+} ion (Figure S15e in the Supporting Information).[51] The lifetime-decay curve taken on monitoring the $^4S_{3/2}\rightarrow{}^4I_{15/2}$ emission at $\lambda=556$ nm (Figure 6j) can be also fitted by a second-order exponential function, thus affording $\tau_1=0.90$ μs (38.98%), $\tau_2=9.12$ μs (61.02%), and $\tau^*=5.92$ μs. The solid-state sample of **1-Tm** emits blue luminescence under excitation at $\lambda=352$ nm and the emission spectrum displays a broad characteristic emission peak at $\lambda=452$ nm due to the $^1D_2\rightarrow{}^3F_4$ transition of the Tm^{3+} ion (Figure 6k). By monitoring the emission at $\lambda=452$ nm, the excitation spectrum shows one peak at $\lambda=352$ nm assigned to the $^3H_6\rightarrow{}^1D_2$ transition of the Tm^{3+} ion (Figure S15f in the Supporting Information). The lifetime-decay curve of **1-Tm** on monitoring the emission at $\lambda=452$ nm (Figure 6l) obeys a second-order exponential function. The resulting lifetime values are $\tau_1=0.93$ μs (37.50%), $\tau_2=8.92$ μs (62.50%), and $\tau^*=5.93$ μs. As mentioned above, the emission spectra of **1-Eu**, **1-Tb**, **1-Dy**, **1-Ho**, **1-Er**, and **1-Tm** display the characteristic emission bands that result from f–f transitions in the RE^{3+} ions. However, from the comparison of the decay curves of **1-Eu**, **1-Tb**, **1-Dy**, **1-Ho**, **1-Er**, and **1-Tm**, it can be clearly seen that the decay curve of **1-Eu** conforms to the single exponential function, thus affording one luminescence lifetime, but the decay curves of **1-Tb**, **1-Dy**, **1-Ho**, **1-Er**, and **1-Tm** obey the second-order exponential function, thus affording two luminescence lifetimes. From the viewpoint of structural chemistry, the molecular-structural units of **1-Eu**, **1-Tb**, **1-Dy**, **1-Ho**, **1-Er**, and **1-Tm** consist of one crystallographically independent RE^{3+} ion and should, therefore, have one luminescence lifetime. According to the longstanding work of Yamase and co-workers,[52] we speculate that the O→W ligand to metal charge transfer (LMCT) transitions of the AT fragments in these structures play an important role in sensitization of the RE^{3+} luminescence. Thus, the emission spectra and luminescence decay–time curves of $K_{14}[As_2W_{19}O_{67}(H_2O)]$ under similar measurement conditions have been carried out because the skeleton of this compound is very similar to the W–O skeletons of **1-Eu**, **1-Tb**, **1-Dy**, **1-Ho**, **1-Er**, and **1-Tm**. Upon different excitations, $K_{14}[As_2W_{19}O_{67}(H_2O)]$ always exhibits a broad emission band centered at approximately $\lambda=510$ nm (Figure S17 in the Supporting Information), which is induced by the $^3T_{1u}\rightarrow{}^1A_{1g}$ transitions derived from the O→W LMCT transitions of ATs.[52] All the lifetime-decay curves of $K_{14}[As_2W_{19}O_{67}(H_2O)]$ are fitted to a double exponential function (Table S7 in the Supporting Information). It can be concluded from these results that the intramolecular transfer of the O→W LMCT energy to the RE^{3+} centers has indeed occurred during the course of the emission process of **1-Tb**, **1-Dy**, **1-Ho**, **1-Er**, and **1-Tm**, thus leading to the appearance of two lifetimes. As we know, the emission intensity of the Eu^{3+} ion is much stronger than the Tb^{3+}, Dy^{3+}, Ho^{3+}, Er^{3+}, or Tm^{3+} ions under similar conditions; moreover, the emission intensity of the Eu^{3+}, Tb^{3+}, Dy^{3+}, Ho^{3+}, Er^{3+}, or Tm^{3+} ions is by far stronger than that of the W–O skeletons in **1-Eu**, **1-Tb**, **1-Dy**, **1-Ho**, **1-Er**, or **1-Tm**. Therefore, the luminescence process of **1-Eu** is principally derived from the Eu^{3+} ion and the lesser contribution of W–O skeletons, which results in **1-Eu** having one lifetime, whereas the luminescence processes of **1-Tb**, **1-Dy**, **1-Ho**, **1-Er**, and **1-Tm** are due to the combined contribution of the RE^{3+} ions and W–O skeletons, which result in two lifetimes.

Similar observations were encountered in our previous studies.[34b,35] Under similar experimental conditions, the solid-state PL properties of **2-Tb**, **2-Dy**, **2-Ho**, **2-Er**, and **2-Tm** were also investigated at room temperature (Figure S18 in the Supporting Information), which were very similar to **1-Tb**, **1-Dy**, **1-Ho**, **1-Er**, and **1-Tm**; furthermore, all of these compounds displayed characteristic emission bands that originate from f–f transitions in RE^{3+} ions. Moreover, the lifetime-decay curves of **2-Tb**, **2-Dy**, **2-Ho**, **2-Er**, and **2-Tm** also follow the second-order exponential function (see Figure S19 and the discussion in the Supporting Information). Similarly, the O→W LMCT transitions of AT fragments in the structures of **2-Tb**, **2-Dy**, **2-Ho**, **2-Er**, and **2-Tm** for the sensitization of the RE^{3+} luminescence have been evidenced by the emission spectra and the lifetime–decay measurements of $Na_{27}[NaAs_4W_{40}O_{140}]\cdot 60\,H_2O$ under similar conditions because the skeleton of this compound is very similar to the W–O backbones of **2-Tb**, **2-Dy**, **2-Ho**, **2-Er**, and **2-Tm** (Figure S20 in the Supporting Information). Furthermore, comparisons of the emission spectra under the same conditions of **1-Tb**, **1-Dy**, **1-Ho**, **1-Er**, and **1-Tm** with **2-Tb**, **2-Dy**, **2-Ho**, **2-Er**, and **2-Tm** reveal that the emission intensities of **2-Tb**, **2-Dy**, **2-Ho**, **2-Er**, and **2-Tm** are greater than **1-Tb**, **1-Dy**, **1-Ho**, **1-Er**, and **1-Tm**, respectively (Figure S21 a–e in the Supporting Information), which is mainly because each RE^{3+} ion in **1** has four coordinated water molecules, whereas each RE^{3+} ion in **2** has three coordinated water molecules. It is well known that the water ligands coordinated to RE^{3+} ions can quench the PL emission intensity to some degree.[45c–d]

In addition, when the solid-state sample of **1-Dy** was excited under UV light of $\lambda = 388$ nm, the near-infrared (NIR) luminescent emission spectrum was obtained. The NIR emission spectrum between $\lambda = 800$ and 1500 nm demonstrates six characteristic peaks at $\lambda = 849$, 927, 994, 1172, 1292, and 1378 nm, which are ascribed to the $^4F_{9/2}\rightarrow{}^6H_{7/2}+{}^6F_{9/2}$, $^4F_{9/2}\rightarrow{}^6H_{5/2}$, $^4F_{9/2}\rightarrow{}^6F_{7/2}$, $^4F_{9/2}\rightarrow{}^6F_{5/2}$, $^6F_{11/2}+{}^6H_{9/2}\rightarrow{}^6H_{15/2}$, and $^4F_{9/2}\rightarrow{}^6F_{1/2}$ transitions of the Dy^{3+} ion, respectively (Figure 7 a).[53] The decay curve of the **1-Dy** by monitoring the emission at $\lambda = 849$ nm upon excitation at $\lambda = 388$ nm can be fitted into a double exponential function. The resulting lifetimes $\tau_1 = 7.56$ μs (86.70%), $\tau_2 = 15.41$ μs (13.30%), and $\tau^* = 8.61$ μs were obtained (Figure 7 b).

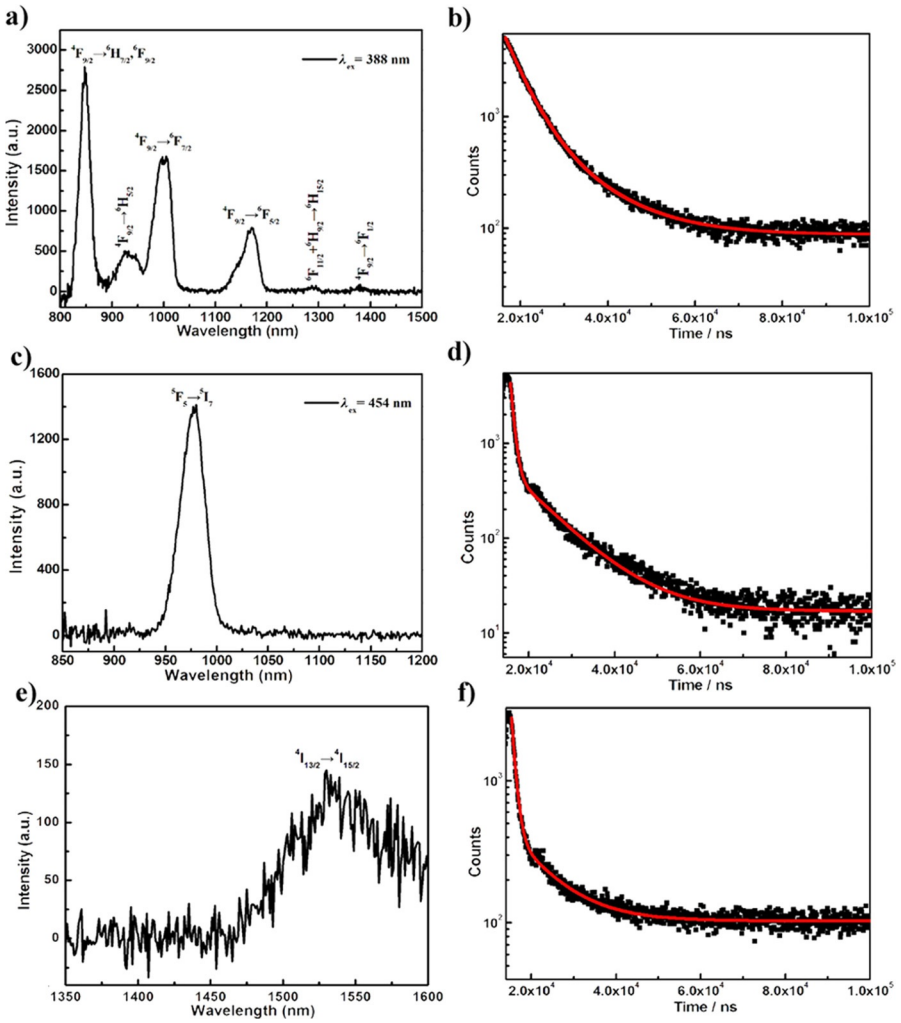

Figure 7. a) The PL emission spectrum of **1-Dy**. b) The lifetime-decay curve of **1-Dy** measured by monitoring the emission at $\lambda = 849$ nm. c) The PL emission spectrum of **1-Ho**. d) The lifetime-decay curve of **1-Ho** measured by monitoring the emission at $\lambda = 974$ nm. e) The PL emission spectrum of **1-Er**. f) The lifetime-decay curve of **1-Er** measured by monitoring the emission at $\lambda = 1530$ nm.

On excitation at $\lambda = 454$ nm, the NIR emission spectrum of **1-Ho** shows a sharp peak at $\lambda = 974$ nm assigned to the $^5F_5 \rightarrow {}^5I_7$ transition of the Ho^{3+} ion (Figure 7c).[54] Monitoring of the luminescent–decay curve at the emission of $\lambda = 974$ nm adheres to a second-order exponential function. The resulting values $\tau_1 = 0.71$ μs (40.12%), $\tau_2 = 9.61$ μs (59.88%), and $\tau^* = 6.36$ μs were obtained (Figure 7d). The NIR emission spectrum of a solid-state sample of **1-Er** on excitation at $\lambda = 381$ nm was also measured, in which a characteristic emission peak at $\lambda = 1536$ nm belongs to the $^4I_{13/2} \rightarrow {}^4I_{15/2}$ transition of the Er^{3+} ion (Figure 7e).[55] The luminescent–decay curve measured by monitoring the emission at $\lambda = 1530$ nm ($^4I_{13/2} \rightarrow {}^4I_{15/2}$) follows a second-order exponential function, thus giving the lifetimes $\tau_1 = 1.04$ μs (46.83%), $\tau_2 = 8.92$ μs (53.17%), and $\tau^* = 5.24$ μs (Figure 7f). Analogously, the NIR PL spectra and decay behaviors of solid-state samples of **1-Dy**, **1-Ho**, and **1-Er** were also measured at room temperature, which are very similar to those of (see Figure S22 and the discussion in the Supporting Information).

A solid-state sample of **3-Pr** emits red luminescence under excitation at $\lambda = 451$ nm and its emission spectrum reveals seven characteristic peaks at $\lambda = 529$, 547, 603, 615, 645, 674, and 729 nm that are attributed to the $^3P_1 \rightarrow {}^3H_5$, $^3P_0 \rightarrow {}^3H_5$, $^7D_2 \rightarrow {}^3H_4$, $^3P_0 \rightarrow {}^3H_6$, $^3P_0 \rightarrow {}^3F_2$, $^3P_1 \rightarrow {}^3F_2$, and $^3P_0 \rightarrow {}^3F_3$ transitions, respectively, of the Pr^{3+} ions (Figure 8a). The excitation spectrum obtained by monitoring the emission at $\lambda = 645$ nm contains three characteristic peaks at $\lambda = 451$ ($^3H_4 \rightarrow {}^3P_2$), 472 ($^3H_4 \rightarrow {}^3P_1$), and 488 nm ($^3H_4 \rightarrow {}^3P_0$; see Figure S23a in the Supporting Information).[56] The decay curve monitored on emission at $\lambda = 645$ nm can be fitted into a double exponential function with $\tau_1 = 0.77$ μs (44.31%), $\tau_2 = 9.65$ μs (55.69%), and $\tau^* = 5.72$ μs (Figure 8b). A solid-state sample of **3-Sm** upon excitation at $\lambda = 402$ nm emits orange luminescence, and its emission spectrum displays four obvious peaks of the Sm^{3+} ions at $\lambda = 402$ nm 560 ($^4G_{5/2} \rightarrow {}^6H_{5/2}$), 597 ($^4G_{5/2} \rightarrow {}^6H_{7/2}$), 642 ($^4G_{5/2} \rightarrow {}^6H_{9/2}$), and 702 nm ($^4G_{5/2} \rightarrow {}^6H_{11/2}$; Figure 8c). These emission peaks stem from an initial population of the $^4D_{7/2}$ state that relaxes nonradiatively to the $^4G_{5/2}$ emitting state, which is induced

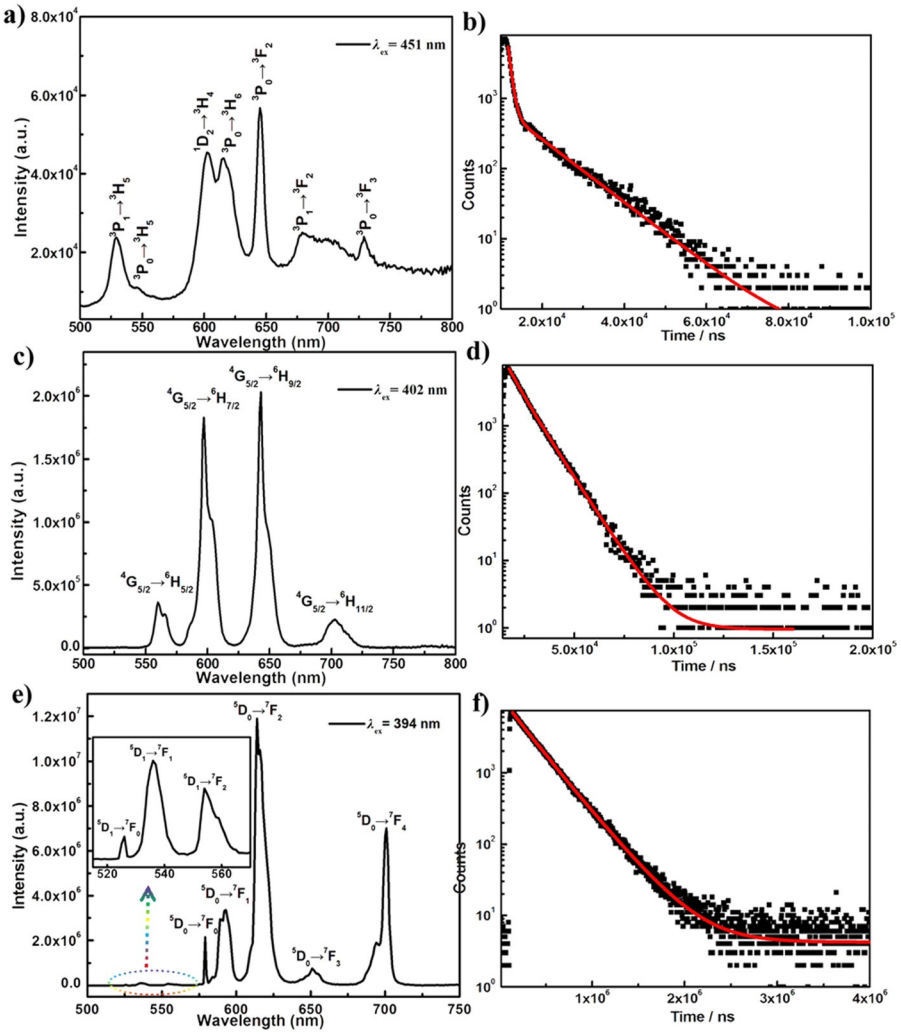

Figure 8. a) The PL emission spectrum of **3-Pr**. b) The luminescence decay curve of **3-Pr** measured by monitoring the emission at $\lambda = 645$ nm. c) The PL emission spectrum of **3-Sm**. d) The luminescence decay curve of **3-Sm** measured by monitoring the emission at $\lambda = 642$ nm. e) The PL emission spectrum of **3-Eu**. f) The luminescence decay curve of **3-Eu** measured by monitoring the emission at $\lambda = 614$ nm.

by the small energy differences among the intermediate states.[57a–c] It is generally known that emissions with $\Delta J=2$ and ± 1 are assigned to MD transitions, whereas emissions with $\Delta J=\leq 6$ when $\Delta J=2$, 4, and 6, except for $J=0$, belong to ED transitions.[57a] Whereby, the emissions at $\lambda=560$, 597, 642, and 702 nm correspond to the MD, partial MD, partial ED, and ED transitions, respectively. In general, the MD $^4G_{5/2}\rightarrow{}^6H_{5/2}$ emission intensity is insensitive to the symmetry of the local environment of the Sm^{3+} ion, whereas the ED $^4G_{5/2}\rightarrow{}^6H_{9/2}$ emission intensity is highly influenced by the local environment. The greater the intensity of the ED transition, the more asymmetric the nature of the local environment is.[56d,e] Thereby, the ED/MD $I(^4G_{5/2}\rightarrow{}^6H_{9/2})/I(^4G_{5/2}\rightarrow{}^6H_{5/2})$ intensity ratio often functions as an indicator of the symmetry of the local environment of the Sm^{3+} ion. In the case of **3-Sm**, the intensity ratio of $I(^4G_{5/2}\rightarrow{}^6H_{9/2})/I(^4G_{5/2}\rightarrow{}^6H_{5/2})$ is approximately 5.7:1, which is strong evidence that the Sm^{3+} ions exist in low-symmetric coordination environments. The excitation spectrum of **3-Sm** exhibits several peaks at $\lambda=346$, 362, 375, 391, 402, 416, 441, 465, 478, 489, and 501 nm, which could be refer to the transitions from the ground state $^6H_{5/2}$ to the excited states ($^4K_{17/2}+{}^4L_{17/2}$, $^4L_{15/2}$, $^6P_{7/2}$, $^4K_{11/2}$, $^4F_{7/2}$, $^6P_{5/2}$, $^4G_{9/2}$, $^4I_{13/2}$, $^4I_{11/2}$, $^4I_{9/2}$, and $^4G_{7/2}$; see Figure S23b in the Supporting Information).[59a,60] The decay–time profile of **3-Sm** measured by monitoring the emission at $\lambda=642$ nm is in agreement with a second-order exponential function, thus providing $\tau_1=5.70$ μs (22.62%), $\tau_2=9.68$ μs (79.38%), and $\tau^*=8.86$ μs (Figure 8d), which gives a slightly longer lifetime relative to the Sm^{3+} compound $[H_2N(CH_3)_2]_6Na_{24}H_{16}\{[Sm_{10}W_{16}(H_2O)_{30}O_{50}](B\text{-}\alpha\text{-}AsW_9O_{33})_8\}\cdot 97\,H_2O$ (i.e., $\tau=8.31$ μs).[35a] Similar to **1-Eu**, the solid-state sample of **3-Eu** emits red luminescence on excitation at $\lambda=394$ nm and exhibits eight emission peaks at $\lambda=526$, 536, 554, 579, 592, 614, 651, and 701 nm (Figure 8e). The excitation spectrum of **3-Eu** on monitoring the emission at $\lambda=614$ nm also presents five featured peaks at $\lambda=363$, 385, 394, 415, and 464 nm that are assigned to the $^7F_0\rightarrow{}^5D_4$, $^7F_0\rightarrow{}^5G_2$, $^7F_0\rightarrow{}^5D_3{}^7$, $F_0\rightarrow{}^5L_6$, and $^7F_0\rightarrow{}^5D_2$ transitions, respectively (Figure S23c in the Supporting Information). The lifetime–decay behavior measured by monitoring the emission at $\lambda=614$ nm agrees with a single exponential function, thus giving $\tau=271.20$ μs (Figure 8f). Under the irradiation of a UV lamp of $\lambda=365$ nm, **3-Eu** also exhibits red luminescence (Figure S16c in the Supporting Information). Careful comparison of the PL properties of **1-Eu** and **3-Eu** leads us to find two differences: 1) The intensity ratio of $I(^5D_0\rightarrow{}^7F_2)/I(^5D_0\rightarrow{}^7F_1)$ is approximately 6.6:1 in **3-Eu**, whereas the intensity ratio of the $I(^5D_0\rightarrow{}^7F_2)/I(^5D_0\rightarrow{}^7F_1)$ is approximately 3.5:1 in **1-Eu**, which makes the emission intensity of **3-Eu** apparently higher than in **1-Eu** (see Figures S16a,c and S21f in the Supporting Information), although the Eu^{3+} compositions (given as percentages) in **3-Eu** and **1-Eu** are almost equal. 2) The luminescence lifetime of **3-Eu** is slightly longer than that of **1-Eu** ($\tau=271.20$ vs. 227.15 μs), for which the dominating reason is that each Eu^{3+} ion possesses four water ligands in **1-Eu** and each Eu^{3+} ion has two coordinated water molecules in **3-Eu**, which results in the stronger emission intensity and the longer luminescence lifetime of **3-Eu** because Ser ligands in the structure of **3-Eu** substitute for water ligands in **1-Eu**, thus leading to a decrease in the number of coordinated water molecules. As we know, water ligands on Eu^{3+} ions can easily enhance the radiationless deactivation of the $^5D_0$ state and partly quench the luminescence emission.[45c–d] In comparison with our recently reported RECATs $[H_2N(CH_3)_2]_6Na_{24}H_{16}\{[Eu_{10}W_{16}(H_2O)_{30}O_{50}](B\text{-}\alpha\text{-}AsW_9O_{33})_8\}\cdot 97\,H_2O$ (**4-Eu**) [35a] and $[H_2N(CH_3)_2]_8Na_8\{[W_3Eu_2(H_2O)_8AsO_8(OH)][B\text{-}\alpha\text{-}AsW_9O_{33}]_2\}_2\cdot 65\,H_2O$ (**5-Eu**),[35b] for which the intensity ratios of $I(^5D_0\rightarrow{}^7F_2)/I(^5D_0\rightarrow{}^7F_1)$ are approximately 5.7:1 and 3.0:1 and the luminescence lifetimes are $\tau=269.12$ and 270.46 μs, respectively, it can be seen that the intensity ratios of $I(^5D_0\rightarrow{}^7F_2)/I(^5D_0\rightarrow{}^7F_1)$ for these compounds are higher than or equal to 3.0:1, thus indicating that the Eu^{3+} ions exist in low-symmetric coordination environments. In addition, the luminescence lifetime of **1-Eu** is the shortest among the four RECATs, which can be because the coordination sphere of the Eu^{3+} ion in **1-Eu** has four water ligands, whereas the coordination spheres of the Eu^{3+} ions in **3-Eu**, **4-Eu**, and **5-Eu** have two or three water ligands. In addition, the luminescence contribution of the O→W LMCT transitions from the W–O skeletons in **3-Pr**, **3-Sm**, and **3-Eu** can be also supported by the emission spectra and the luminescence–decay curves of $Na_{27}[NaAs_4W_{40}O_{140}]\cdot 60\,H_2O$ under similar conditions (Figure S24 in the Supporting Information).

The NIR emission spectra and decay–time profiles of the solid-state samples of **3-Pr**, **3-Nd**, and **3-Sm** have been also investigated at room temperature. On excitation at $\lambda=451$ nm, the NIR emission spectrum of **3-Pr** consists of two characteristic peaks of the Pr^{3+} ions at $\lambda=859$ ($^1D_2\rightarrow{}^3F_2$) and 1021 nm ($^1D_2\rightarrow{}^3F_4$; Figure 9a).[54] The monitoring of the luminescent–decay curve of the emission at $\lambda=1021$ nm ($^1D_2\rightarrow{}^3F_4$) can be fitted to a second-order exponential function, thus giving $\tau_1=0.68$ μs (27.68%), $\tau_2=9.01$ μs (72.32%), and $\tau^*=6.70$ μs (Figure 9b). On excitation at $\lambda=584$ nm, the NIR emission spectrum of **3-Nd** shows three bands at $\lambda=893$, 1057, and 1331 nm assigned to the $^4F_{3/2}\rightarrow{}^4I_{9/2}$, $^4F_{3/2}\rightarrow{}^4I_{11/2}$, and $^4F_{3/2}\rightarrow{}^4I_{13/2}$ transitions of the Nd^{3+} ions (Figure 9c). Furthermore, the excitation spectrum of **3-Nd** monitored at an emission of $\lambda=1057$ nm mainly demonstrates six excitation peaks at $\lambda=475$ ($^4I_{9/2}\rightarrow{}^2G_{9/2}+{}^4G_{11/2}+{}^2K_{15/2}$), 524 ($^4I_{9/2}\rightarrow{}^4G_{7/2}+{}^4G_{9/2}+{}^2K_{13/2}$), 584 ($^4I_{9/2}\rightarrow{}^2G_{7/2}+{}^4G_{5/2}$), 629 ($^4I_{9/2}\rightarrow{}^2H_{11/2}$), 684 ($^4I_{9/2}\rightarrow{}^4H_{9/2}$), and 746 nm ($^4I_{9/2}\rightarrow{}^4S_{3/2}+{}^4F_{7/2}$; see Figure S22d in the Supporting Information).[59] The decay curve of **3-Nd** was recorded by monitoring the emission at $\lambda=1057$ nm ($^4F_{3/2}\rightarrow{}^4I_{11/2}$) and was fitted into a second-order exponential function, thus giving $\tau_1=1.03$ μs (19.26%), $\tau_2=10.35$ μs (80.74%), and $\tau^*=8.55$ μs (Figure 9d). On excitation at $\lambda=402$ nm, the NIR emission spectrum of **3-Sm** shows four groups of characteristic bands of the Sm^{3+} ions centered at $\lambda=895$ ($^4G_{5/2}\rightarrow{}^6F_{3/2}$), 940 ($^4G_{5/2}\rightarrow{}^6F_{5/2}$), 1022 ($^4G_{5/2}\rightarrow{}^6F_{7/2}$), and 1165 nm ($^4G_{5/2}\rightarrow{}^6F_{9/2}$) (Figure 9e). The decay curve of **3-Nd** can be fitted into a second-order exponential function with $\tau_1=6.84$ μs (54.45%), $\tau_2=10.97$ μs (45.55%), and $\tau^*=8.72$ μs (Figure 9f). As far as we know, **2-Dy**, **2-Ho**, **2-Er**, **3-Pr**, **3-Nd**, and **3-Sm** represent the rare examples of the NIR luminescent emission properties of POM-based materials.

The CIE 1931 diagram is a worldwide, useful approach to assess all the possible color outcomes, by combining three pri-

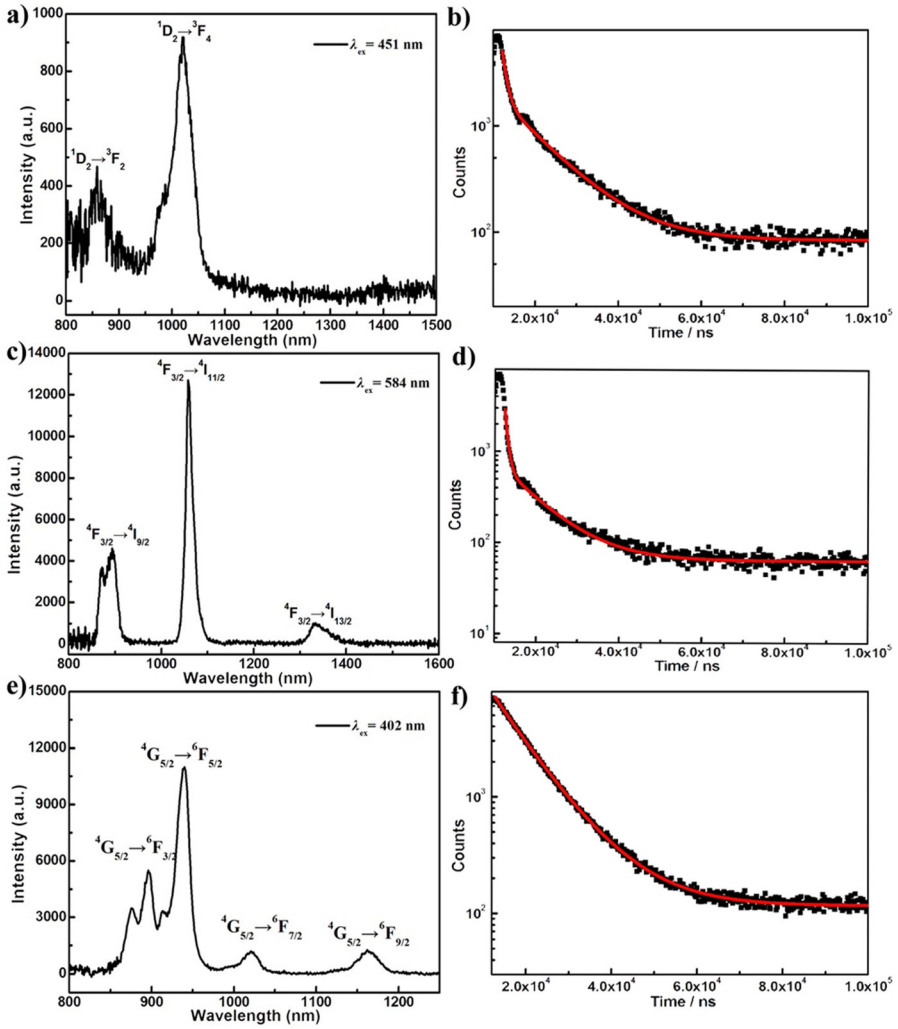

Figure 9. a) The PL emission spectrum of **3-Pr**. b) The luminescence decay curve of **3-Pr** measured by monitoring the emission at $\lambda = 1021$ nm. c) The PL emission spectrum of **3-Nd**. d) The luminescence-decay curve of **3-Nd** measured by monitoring the emission at $\lambda = 1057$ nm. e) The PL emission spectrum of **3-Sm**. f) The luminescence-decay curve of **3-Sm** measured by monitoring the emission at $\lambda = 940$ nm.

mary colors, in which the chromaticity coordinates *x* and *y* are used to determine the exact emission colors of the as-prepared materials.[60,61] The dominant wavelength can be defined as a monochromatic wavelength that appears to be the same color as the light source. On the CIE color-coordinate space, a straight line drawn between the white point and the point that corresponds to the color of the illuminant can be extra polated to intersect the perimeter of the space at two points. The point of intersection nearer to the color in question reveals the dominant wavelength of the color as the wavelength of the pure spectral color at that intersection point.[62] Furthermore, the color purity is the weighted average of the coordinate (*x*, *y*) relative to the coordinate of the illuminant and the coordinate of the dominant wavelength.[63] Thus, the color purity can be described with Equation (1):

$$\text{color purity} = \frac{\sqrt{(x-x_i)^2+(y-y_i)^2}}{\sqrt{(x_d-x_i)^2+(y_d-y_i)^2}} = 100\% \qquad (1)$$

The CIE chromaticity coordinates for **1-Eu**, **1-Tb**, **1-Dy**, **1-Ho**, **1-Er**, and **1-Tm** are determined on the basis of their corresponding visible PL spectra and are indexed to (0.6493, 0.3501), (0.3289, 0.5913), (0.3876, 0.4391), (0.5741, 0.4247), (0.4449, 0.5197), and (0.2410, 0.2703), respectively (Figure 10). The dominant wavelength of **1-Eu** is $\lambda = 605$ nm, the chromaticity coordinate (0.6493, 0.3501) is located in the pure-red region, and the calculated color purity of **1-Eu** is 100.00%. It is easy to understand that **1-Eu** has a good color purity because the location of the color coordinates of its red-light emission is close to the spectral edge of the 1931 CIE chromatic diagram as a result of the dominant $^5D_0 \rightarrow {}^7F_2$ transition of the Eu^{3+} ion. In addition, the calculated color temperature is 2351 K. Similarly, the dominant wavelengths of **1-Tb**, **1-Dy**, **1-Ho**, **1-Er**, and **1-Tm** are $\lambda = 553$, 570, 590, 572, and 482 nm, respectively. In addition, the calculated color purities of **1-Tb**, **1-Dy**, **1-Ho**, **1-Er**, and **1-Tm** are 76.12, 48.05, 99.71, 89.75, and 36.61%, respectively, and the correlated color temperatures of these compounds are 5569, 4185, 1800, 3600, and 17625 K, respectively.

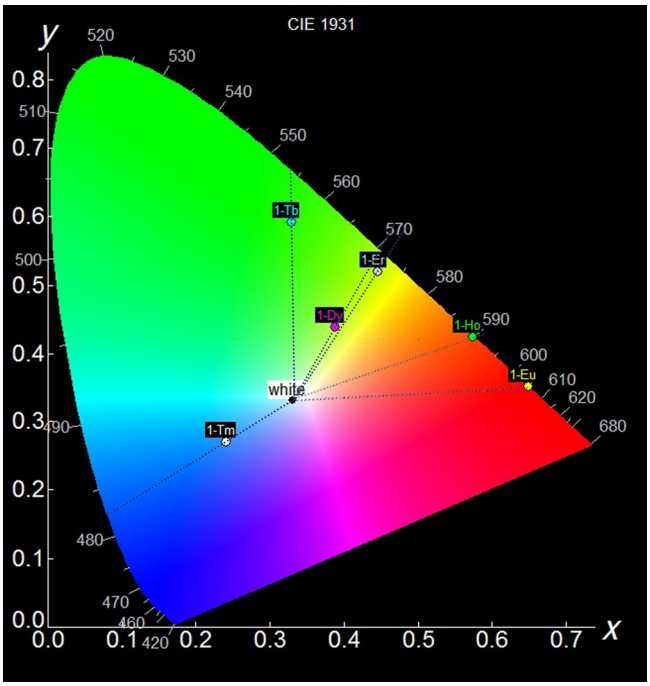

Figure 10. The CIE chromaticity diagram of the emissions of **1-Eu**, **1-Tb**, **1-Dy**, **1-Ho**, **1-Er**, and **1-Tm**.

The CIE chromaticity coordinates for **2-Tb**, **2-Dy**, **2-Ho**, **2-Er**, and **2-Tm**, based on their corresponding visible PL spectra, are (0.3294, 0.5926), (0.3901, 0.4421), (0.6254, 0.3738), (0.3835, 0.5636), and (0.2136, 0.2142), respectively (Figure S25 in the Supporting Information). The dominant wavelengths of **2-Tb**, **2-Dy**, **2-Ho**, **2-Er**, and **2-Tm** are $\lambda = 553$, 570, 600, 563, and 477 nm, respectively; the calculated color purities of these compounds are 76.50, 49.60, 99.53, 85.07, and 52.01 %, respectively; and the correlated color temperatures are 5560, 4146, 1828, 4651, and 130 763 K, respectively. The CIE chromaticity coordinates for **3-Pr**, **3-Sm**, and **3-Eu**, based on their corresponding visible PL spectra, are (0.5382, 0.4492), (0.6057, 0.3931), and (0.6481, 0.3513), respectively (Figure S26 in the Supporting Information); the dominant wavelengths of these compounds are $\lambda = 585$, 596, and 605 nm, respectively; the calculated color purities are 96.62, 99.41, and 99.97 %, respectively; and the correlated color temperatures are 2150, 1687, and 2311 K, respectively.

In addition, the CIE chromaticity comparisons for **1-Eu**, **1-Tb**, **1-Dy**, **1-Ho**, **1-Er**, **1-Tm**, **2-Tb**, **2-Dy**, **2-Ho**, **2-Er**, **2-Tm**, **3-Pr**, **3-Sm**, and **3-Eu** with the corresponding $RE(NO_3)_3{\cdot}6H_2O$ are displayed in Figures S27–S29 in the Supporting Information. The non-superposition of their CIE chromaticity coordinates with those values of the corresponding $RE(NO_3)_3{\cdot}6H_2O$ suggests, to some degree, the existence of the intramolecular transfer of the O→W LMCT energy to the RE^{3+} centers in the luminescence processes of **1-Eu**, **1-Tb**, **1-Dy**, **1-Ho**, **1-Er**, **1-Tm**, **2-Tb**, **2-Dy**, **2-Ho**, **2-Er**, **2-Tm**, **3-Pr**, **3-Sm**, and **3-Eu**.

Conclusions

Three types of serine-decorated RECAT **1**–**3** have been prepared, with the participation of two organic solubilizers under laboratory conditions, and structurally characterized. The polyoxoanion of type **1** revealed a novel dual-Ser-participating di-RE^{3+}-incorporated dimeric sandwich-type assembly, whereas the polyoxoanions of types **2** and **3** demonstrate the dual-/tetra-Ser-participating tetra-RE^{3+}-incorporated tetrameric square structure. Most interestingly, RE^{3+} ions played an important role in the structural construction and the luminescence properties of the desired products; furthermore, variation in the amount of the RE^{3+} salts used led to a structural transformation from dimerization to tetramerization of Ser-decorated RECATs. Such an observation has been extremely rarely encountered in POM chemistry. The solid-state visible and NIR PL properties and lifetime–decay behaviors of some of the representative compounds have been systematically examined. Moreover, the dominant wavelengths, color purities, and correlated color temperatures of these representative compounds have been also calculated. The successful preparations of these Ser-decorated RECATs not only exemplify the feasibility of this one-step self-assembly strategy in the synthesis of novel organic–inorganic hybrid RECAT aggregates by the synergistic effect of two organic solubilizers, but also can provide some beneficial guidance and enlightenment for extending the potential of RE-substituted POMs in the field of luminescent materials. In continuing work, other heteroatoms, such as Sb^{III}, Bi^{III}, Se^{IV}, and Te^{IV} and other combination pairs of organic solubilizers, including different N,O-containing carboxylate or chiral amino acid ligands, will be introduced into our research to investigate and discover much more organic–inorganic hybrid RE-substituted POMs with intriguing structures and properties. Furthermore, we will intensively investigate the reaction parameters and key controllable factors in the structural construction of POMs.

Acknowledgements

This work was supported by the Natural Science Foundation of China (21671054, 21301049, U1304208, 21571048), the Program for Science & Technology Innovation Talents in Universities of Henan Province (16HASTIT001), the Innovation Scientists and Technicians Troop Construction Projects of Henan Province (174100510016), the Natural Science Foundation of Henan Province (142300410451), the Postdoctoral Foundation of Henan Province (20140025), the Foundation of State Key Laboratory of Structural Chemistry (20160016), the 2014 Special Foundation for Scientific Research Project of Henan University (XXJC20140001), the Foundation of Education Department of Henan Province (16A150027), and the 2016 Students Innovative Pilot Plan of Henan University (16NA005).

Keywords: arsenotungstates · luminescence · polyoxometalates · rare earths · self-assembly

[1] a) J. Marrot, M. A. Pilette, M. Haouas, S. Floquet, F. Taulelle, X. López, J. M. Poblet, E. Cadot, *J. Am. Chem. Soc.* **2012**, *134*, 1724; b) Y. Zhao, D.-S. Deng, L.-F. Ma, B.-M. Ji, L.-Y. Wang, *Chem. Commun.* **2013**, *49*, 10299; c) J. Heine, K. Müller-Buschbaum, *Chem. Soc. Rev.* **2013**, *42*, 9232; d) A. B. Descalzo, R. Martínez-Máñez, F. Sancenón, K. Hoffmann, K. Rurack, *Angew. Chem. Int. Ed.* **2006**, *45*, 5924; *Angew. Chem.* **2006**, *118*, 6068; e) S.-T. Zheng, J. Zhang, X.-X. Li, W.-H. Fang, G.-Y. Yang, *J. Am. Chem. Soc.* **2010**, *132*, 15102; f) B. Artetxe, S. Reinoso, L. S. Felices, L. Lezama, J. M. Gutiérrez-Zorrilla, J. A. García, J. R. Galán-Mascarós, A. Haider, U. Kortz, C. Vicent, *Chem. Eur. J.* **2014**, *20*, 12144.

[2] a) J. M. Clemente-Juan, E. Coronado, A. Gaita-Ariño, *Chem. Soc. Rev.* **2012**, *41*, 7464; b) D.-L. Long, R. Tsunashima, L. Cronin, *Angew. Chem. Int. Ed.* **2010**, *49*, 1736; *Angew. Chem.* **2010**, *122*, 1780; c) Y.-F. Song, R. Tsunashima, *Chem. Soc. Rev.* **2012**, *41*, 7384.

[3] F. Hussain, R. W. Gable, M. Speldrich, P. Kögerler, C. Boskovic, *Chem. Commun.* **2009**, 328.

[4] C. Ritchie, C. Boskovic, *Cryst. Growth Des.* **2010**, *10*, 488.

[5] C. Ritchie, E. G. Moore, M. Speldrich, P. Kögerler, C. Boskovic, *Angew. Chem. Int. Ed.* **2010**, *49*, 7702; *Angew. Chem.* **2010**, *122*, 7868.

[6] C. Ritchie, M. Speldrich, R. W. Gable, L. Sorace, P. Kögerler, C. Boskovic, *Inorg. Chem.* **2011**, *50*, 7004.

[7] C. Ritchie, C. E. Miller, C. Boskovic, *Dalton Trans.* **2011**, *40*, 12037.

[8] C. Ritchie, V. Baslon, E. G. Moore, C. Reber, C. Boskovic, *Inorg. Chem.* **2012**, *51*, 1142.

[9] M. Vonci, F. A. Bagherjeri, P. D. Hall, R. W. Gable, A. Zavras, R. A. J. O'Hair, Y. P. Liu, J. Zhang, M. R. Field, M. B. Taylor, J. D. Plessis, G. Bryant, M. Riley, L. Sorace, P. A. Aparicio, X. López, J. M. Poblet, C. Ritchie, C. Boskovic, *Chem. Eur. J.* **2014**, *20*, 14102.

[10] J.-Y. Niu, X. Ma, J.-W. Zhao, P.-T. Ma, C. Zhang, J.-P. Wang, *CrystEngComm* **2011**, *13*, 4834.

[11] Z. Zhou, D. D. Zhang, L. Yang, P. T. Ma, Y. N. Si, U. Kortz, J. Y. Niu, J. P. Wang, *Chem. Commun.* **2013**, *49*, 5189.

[12] S. Z. Li, Y. Wang, P. T. Ma, J. P. Wang, J. Y. Niu, *CrystEngComm* **2014**, *16*, 10746.

[13] Y. H. Zhang, D. D. Zhang, Z. Y. Huo, P. T. Ma, J. Y. Niu, J. P. Wang, *RSC Adv.* **2014**, *4*, 28848.

[14] Y. Wang, X. P. Sun, S. Z. Li, P. T. Ma, J. P. Wang, J. Y. Niu, *Dalton Trans.* **2015**, *44*, 733.

[15] Y. Wang, X. P. Sun, S. Z. Li, P. T. Ma, J. Y. Niu, J. P. Wang, *Cryst. Growth Des.* **2015**, *15*, 2057.

[16] P. T. Ma, R. Wan, Y. N. Si, F. Hu, Y. Y. Wang, J. Y. Niu, J. P. Wang, *Dalton Trans.* **2015**, *44*, 11514.

[17] Y. Huo, Z. Y. Huo, P. T. Ma, J. P. Wang, J. Y. Niu, *Inorg. Chem.* **2015**, *54*, 406.

[18] L. Yang, X. Ma, P. T. Ma, J. A. Hua, J. Y. Niu, *Cryst. Growth Des.* **2013**, *13*, 2982.

[19] F. Hussain, U. Kortz, R. J. Clark, *Inorg. Chem.* **2004**, *43*, 3237.

[20] F. Hussain, U. Kortz, *Chem. Commun.* **2005**, 1191.

[21] K.-Y. Wang, B. S. Bassil, Z.-G. Lin, A. Haider, J. Cao, H. Stephan, K. Viehweger, U. Kortz, *Dalton Trans.* **2014**, *43*, 16143.

[22] F. Hussain, F. Conrad, G. R. Patzke, *Angew. Chem. Int. Ed.* **2009**, *48*, 9088; *Angew. Chem.* **2009**, *121*, 9252.

[23] F. Hussain, B. Spingler, F. Conrad, M. Speldrich, P. Kogerler, C. Boskovic, G. R. Patzke, *Dalton Trans.* **2009**, 4423.

[24] F. Hussain, G. R. Patzke, *CrystEngComm* **2011**, *13*, 530.

[25] W. L. Chen, Y. G. Li, Y. H. Wang, E. B. Wang, Z. M. Su, *Dalton Trans.* **2007**, 4293.

[26] W. L. Chen, Y. G. Li, Y. H. Wang, E. B. Wang, Z. M. Zhang, *Dalton Trans.* **2008**, 865.

[27] X.-J. Feng, H.-Y. Han, Y.-H. Wang, L.-L. Li, Y.-G. Li, E.-B. Wang, *CrystEngComm* **2013**, *15*, 7267.

[28] K. Wassermann, M. H. Dickman, M. T. Pope, *Angew. Chem. Int. Ed. Engl.* **1997**, *36*, 1445; *Angew. Chem.* **1997**, *109*, 1513.

[29] K. Wassermann, M. P. Pope, *Inorg. Chem.* **2001**, *40*, 2763.

[30] K. Fukaya, T. Yamase, *Angew. Chem. Int. Ed.* **2003**, *42*, 654; *Angew. Chem.* **2003**, *115*, 678.

[31] I. M. Mbomekalle, B. Keita, M. Nierlich, U. Kortz, P. Berthet, L. Nadjo, *Inorg. Chem.* **2003**, *42*, 5143.

[32] J. W. Zhao, D. Y. Shi, L. J. Chen, P. T. Ma, J. P. Wang, J. Y. Niu, *CrystEngComm* **2011**, *13*, 3462.

[33] J. W. Zhao, D. Y. Shi, L. J. Chen, X. M. Cai, Z. Q. Wang, P. T. Ma, J. P. Wang, J. Y. Niu, *CrystEngComm* **2012**, *14*, 2797.

[34] a) D.-Y. Shi, J.-W. Zhao, L.-J. Chen, P.-T. Ma, J.-P. Wang, J.-Y. Niu, *CrystEngComm* **2012**, *14*, 3108; b) L. J. Chen, F. Zhang, X. Ma, J. Luo, J. W. Zhao, *Dalton Trans.* **2015**, *44*, 12598.

[35] a) J.-W. Zhao, H.-L. Li, X. Ma, Z. G. Xie, L.-J. Chen, Y. S. Zhu, *Sci. Rep.* **2016**, *6*, 26406; b) H. L. Li, Y. J. Liu, R. Zheng, L. J. Chen, J.-W. Zhao, G.-Y. Yang, *Inorg. Chem.* **2016**, *55*, 3881.

[36] a) I. D. Brown, D. Altermatt, *Acta Crystallogr. Sect. B* **1985**, *41*, 244; b) A. Trzesowska, R. Kruszynski, T. J. Bartczak, *Acta Crystallogr. Sect. B* **2004**, *60*, 174.

[37] a) C. Tourné, A. Revel, G. Tourné, M. Vendrell, *C. R. Acad. Sci. Ser. III* **1973**, *277*, 643; b) U. Kortz, M. G. Savelieff, B. S. Bassil, M. H. Dickman, *Angew. Chem. Int. Ed.* **2001**, *40*, 3384; *Angew. Chem.* **2001**, *113*, 3488.

[38] a) B. M. van der Ende, L. Aarts, A. Meijerink, *Phys. Chem. Chem. Phys.* **2009**, *11*, 11081; b) H. Dong, L.-D. Sun, C.-H. Yan, *Chem. Soc. Rev.* **2015**, *44*, 1608; c) F. S. Richardson, *Chem. Rev.* **1982**, *82*, 541; d) S. J. A. Pope, B. J. Coe, S. Faulkner, E. V. Bichenkova, X. Yu, K. T. Douglas, *J. Am. Chem. Soc.* **2004**, *126*, 9490; e) J. C. G. Bünzli, C. Piguet, *Chem. Soc. Rev.* **2005**, *34*, 1048.

[39] J.-C. G. Bünzli, S. V. Eliseeva, *Chem. Sci.* **2013**, *4*, 1939.

[40] Y. J. Cui, Y. F. Yue, G. D. Qian, B. L. Chen, *Chem. Rev.* **2012**, *112*, 1126.

[41] C.-G. Ma, M. G. Brik, D.-X. Liu, B. Feng, Y. Tian, A. Suchocki, *J. Lumin.* **2016**, *170*, 369.

[42] a) E. G. Moore, A. P. S. Samuel, K. N. Raymond, *Acc. Chem. Res.* **2009**, *42*, 542; b) J.-C. G. Bünzli, *Chem. Rev.* **2010**, *110*, 2729; c) G. J. Sopasis, M. Orfanoudaki, P. Zarmpas, A. Philippidis, M. Siczek, T. Lis, J. R. O'Brien, C. J. Milios, *Inorg. Chem.* **2012**, *51*, 1170.

[43] F. N. Shi, J. Meng, Y. F. Ren, Q. Su, *J. Mater. Chem.* **1997**, *7*, 773.

[44] a) T. R. Zhang, C. Spitz, M. Antonietti, C. F. J. Faul, *Chem. Eur. J.* **2005**, *11*, 1001; b) J.-C. G. Bünzli, G. R. Choppin, *Lanthanide Probes in Life, Chemical, and Earth Sciences: Theory and Practice*, Elsevier **1989**.

[45] a) X. Shen, B. Yan, *J. Mater. Chem. C* **2015**, *3*, 7038; b) R. A. D. de Jesus, L. L. D. Luz, D. O. Santos, J. A. S. Costa, S. Navickiene, C. C. Gatto, S. A. Júnior, M. E. D. Mesquita, *Dalton Trans.* **2015**, *44*, 17318; c) P. Mialane, L. Lisnard, A. Mallard, J. Marrot, E. Antic-Fidancev, P. Aschehoug, D. Vivien, F. Sécheresse, *Inorg. Chem.* **2003**, *42*, 2102; d) J.-W. Zhao, J. Cao, Y.-Z. Li, J. Zhang, L.-J. Chen, *Cryst. Growth Des.* **2014**, *14*, 6217.

[46] a) A. P. S. Samuel, J. D. Xu, K. N. Raymond, *Inorg. Chem.* **2009**, *48*, 687; b) X. J. Zhou, X. Q. Zhao, Y. J. Wang, B. Wu, J. Shen, L. Li, Q. X. Li, *Inorg. Chem.* **2014**, *53*, 12275.

[47] a) M. Xin, D. T. Tu, H. M. Zhu, W. Q. Luo, Z. G. Liu, P. Huang, R. F. Li, Y. G. Cao, X. Y. Chen, *J. Mater. Chem. C* **2015**, *3*, 7286; b) Y. I. Choi, Y. Yoon, J.-G. Kang, Y. Sohn, *J. Lumin.* **2015**, *158*, 27.

[48] a) P. L. Li, Z. J. Wang, Z. P. Yang, Q. L. Guo, *Opt. Commun.* **2014**, *332*, 83; b) J. Zhou, Z. G. Xia, *J. Mater. Chem. C* **2015**, *3*, 7552; c) G. Z. Li, Z. L. Wang, M. Yu, Z. W. Quan, J. Lin, *J. Solid State Chem.* **2006**, *179*, 2698.

[49] a) Z. L. Fu, W. W. Xia, Q. Li, X. Y. Cui, W. H. Li, *CrystEngComm* **2012**, *14*, 4618; b) Y. Zhang, W. T. Gong, J. J. Yu, H. C. Pang, Q. Song, G. L. Ning, *RSC Adv.* **2015**, *5*, 62527.

[50] a) M. Guan, H. Zheng, Z. H. Huang, B. Ma, M. S. Molokeev, S. F. Huang, L. F. Mei, *RSC Adv.* **2015**, *5*, 59403; b) J. Zmojda, M. Kochanowicz, P. Miluski, J. Dorosz, J. Pisarska, W. A. Pisarski, D. Dorosz, *J. Lumin.* **2016**, *170*, 795.

[51] a) Y. Liu, Y. X. Liu, G. X. Liu, X. T. Dong, J. X. Wang, *RSC Adv.* **2015**, *5*, 97995; b) D. He, C. F. Guo, S. Zhou, L. L. Zhang, Z. Yang, C. K. Duan, M. Yin, *CrystEngComm* **2015**, *17*, 7745.

[52] a) T. Yamase, *Chem. Rev.* **1998**, *98*, 307; b) T. Yamase, T. Kobayashi, M. Sugeta, H. Naruke, *J. Phys. Chem. A* **1997**, *101*, 5046; c) T. Ito, H. Yashiro, T. Yamase, *Langmuir* **2006**, *22*, 2806.

[53] J. Feng, L. Zhou, S.-Y. Song, Z.-F. Li, W.-Q. Fan, L.-N. Sun, Y.-N. Yu, H.-J. Zhang, *Dalton Trans.* **2009**, 6593.

[54] S. Dang, J. B. Yu, X. F. Wang, L. N. Sun, R. P. Deng, J. Feng, W. Q. Fan, H. J. Zhang, *J. Lumin.* **2011**, *131*, 1857.

[55] D. Wawrzynczyk, D. Piatkowski, S. Mackowski, M. Samoca, M. Nyk, *J. Mater. Chem. C* **2015**, *3*, 5332.

[56] a) H.-L. Cui, S.-Z. Zhan, M. Li, S. W. Ng, D. Li, *Dalton Trans.* **2011**, *40*, 6490; b) L.-L. Li, R. Pan, J.-W. Zhao, B.-F. Yang, G.-Y. Yang, *Dalton Trans.* **2016**, *45*, 11628; c) L. Bokatial, S. Rai, *J. Lumin.* **2010**, *130*, 1857.

[57] a) A. N. Meza-Rocha, A. Speghini, M. Bettinelli, U. Caldiño, *J. Lumin.* **2015**, *167*, 305; b) U. Caldiño, A. Speghini, S. Berneschi, M. Bettinelli, M.

Brenci, S. Pelli, G. C. Righini, *Opt. Mater.* **2012**, *34*, 1067; c) G. Lakshminarayana, R. Yang, M. Mao, J. Qiu, I. V. Kityk, *J. Non-Cryst. Solids* **2009**, *355*, 2668; d) B. C. Jamalaiah, J. S. Kumar, A. M. Babu, T. Suhaini, L. R. Moorthy, *J. Lumin.* **2009**, *129*, 363; e) Z. G. Xia, D. M. Chen, *J. Am. Ceram. Soc.* **2010**, *93*, 1074.

[58] A. Durairajan, D. Balaji, K. K. Rasu, S. M. Babu, M. A. Valente, D. Thangaraju, Y. Hayakawa, *J. Lumin.* **2016**, *170*, 743.

[59] S. Chorazy, K. Nakabayashi, M. Arczynski, R. Pełka, S. Ohkoshi, B. Sieklucka, *Chem. Eur. J.* **2014**, *20*, 7144.

[60] G. B. Stringfellow, M. G. Craford, *High Brightness Light Emitting Diodes*, Academic Press, **1997**, p. 247.

[61] R. Yu, H. M. Noh, B. K. Moon, B. C. Choi, J. H. Jeong, H. S. Lee, K. Jang, S. S. Yi, *J. Lumin.* **2014**, *152*, 133.

[62] R. S. Harold, *Adapting CIE Specifications to Object Colors*, 2nd ed., Wiley, New York, **1987**, p. 111.

[63] J. Suresh Kumar, K. Pavani, A. M. Babu, N. K. Giri, S. B. Rai, L. R. Moorthy, *J. Lumin.* **2010**, *130*, 1916.

Manuscript received: October 30, 2016
Accepted Article published: December 16, 2016
Final Article published: January 27, 2017